Monthly Notices
of the
ROYAL ASTRONOMICAL SOCIETY

MNRAS **467,** 3140–3159 (2017)
Advance Access publication 2017 January 25

doi:10.1093/mnras/stx201

Angular momentum evolution of galaxies over the past 10 Gyr: a MUSE and KMOS dynamical survey of 400 star-forming galaxies from $z = 0.3$ to 1.7

A. M. Swinbank,[1,2]★ C. M. Harrison,[1,2] J. Trayford,[1,2] M. Schaller,[1,2] Ian Smail,[1,2] J. Schaye,[3] T. Theuns,[1,2] R. Smit,[1,2] D. M. Alexander,[1,2] R. Bacon,[4] R. G. Bower,[1,2] T. Contini,[5,6] R. A. Crain,[7] C. de Breuck,[8] R. Decarli,[9] B. Epinat,[5,6,10] M. Fumagalli,[1,2] M. Furlong,[1,2] A. Galametz,[11] H. L. Johnson,[1,2] C. Lagos,[12,13,14] J. Richard,[4] J. Vernet,[8] R. M. Sharples,[1,2] D. Sobral[15] and J. P. Stott[1,2,16]

Affiliations are listed at the end of the paper

Accepted 2017 January 20. Received 2017 January 20; in original form 2016 July 13

ABSTRACT

We present a MUSE (Multi-Unit Spectroscopic Explorer) and KMOS (*K*-band Multi-Object Spectrograph) dynamical study 405 star-forming galaxies at redshift $z = 0.28$–1.65 (median redshift $\bar{z} = 0.84$). Our sample is representative of the star-forming 'main sequence', with star formation rates of SFR $= 0.1$–30 M$_\odot$ yr^{-1} and stellar masses $M_\star = 10^8$–10^{11} M$_\odot$. For 49 ± 4 per cent of our sample, the dynamics suggest rotational support, 24 ± 3 per cent are unresolved systems and 5 ± 2 per cent appear to be early-stage major mergers with components on 8–30 kpc scales. The remaining 22 ± 5 per cent appear to be dynamically complex, irregular (or face-on systems). For galaxies whose dynamics suggest rotational support, we derive inclination-corrected rotational velocities and show that these systems lie on a similar scaling between stellar mass and specific angular momentum as local spirals with $j_\star = J/M_\star \propto M_\star^{2/3}$ but with a redshift evolution that scales as $j_\star \propto M_\star^{2/3}(1+z)^{-1}$. We also identify a correlation between specific angular momentum and disc stability such that galaxies with the highest specific angular momentum ($\log(j_\star/M_\star^{2/3}) > 2.5$) are the most stable, with Toomre $Q = 1.10 \pm 0.18$, compared to $Q = 0.53 \pm 0.22$ for galaxies with $\log(j_\star/M_\star^{2/3}) < 2.5$. At a fixed mass, the *Hubble Space Telescope* morphologies of galaxies with the highest specific angular momentum resemble spiral galaxies, whilst those with low specific angular momentum are morphologically complex and dominated by several bright star-forming regions. This suggests that angular momentum plays a major role in defining the stability of gas discs: at $z \sim 1$, massive galaxies that have discs with low specific angular momentum are globally unstable, clumpy and turbulent systems. In contrast, galaxies with high specific angular momentum have evolved into stable discs with spiral structure where star formation is a local (rather than global) process.

Key words: galaxies: evolution – galaxies: high-redshift.

1 INTRODUCTION

Identifying the dominant physical processes that were responsible for the formation of the Hubble sequence has been one of the major goals of galaxy formation for decades (Roberts 1963; Gallagher & Hunter 1984; Sandage 1986). Morphological surveys of high-redshift galaxies, in particular utilizing the high angular resolution of the *Hubble Space Telescope* (*HST*), have suggested that only at $z \sim 1.5$ did the Hubble sequence begin to emerge (e.g. Bell et al. 2004; Conselice et al. 2011), with the spirals and ellipticals becoming as common as peculiar galaxies (e.g. Buitrago et al. 2013; Mortlock et al. 2013). However, galaxy morphologies reflect the complex (non-linear) processes of gas accretion, baryonic dissipation, star formation and morphological transformation that have occurred during the history

★ E-mail: a.m.swinbank@dur.ac.uk

of the galaxy. Furthermore, morphological studies of high-redshift galaxies are subject to *K*-corrections and structured dust obscuration, which complicates their interpretation.

The more fundamental physical properties of galaxies are their mass, energy and angular momentum, since these are related to the amount of material in a galaxy, the linear size and the rotational velocity. As originally suggested by Sandage, Freeman & Stokes (1970), the Hubble sequence of galaxy morphologies appears to follow a sequence of increasing angular momentum at a fixed mass (e.g. Fall 1983; Fall & Romanowsky 2013; Obreschkow & Glazebrook 2014). One route to identifying the processes responsible for the formation of discs is therefore to measure the evolution of the mass, size and dynamics (and hence angular momentum) of galaxy discs with cosmic time – properties that are more closely related to the underlying dark matter halo.

In the cold dark matter (CDM) paradigm, baryonic discs form at the centres of dark matter haloes. As dark matter haloes grow early in their formation history, they acquire angular momentum (J) as a result of large-scale tidal torques. The angular momentum acquired has strong mass dependence, with $J \propto M_{\rm halo}^{5/3}$ (e.g. Catelan & Theuns 1996). Although the haloes acquire angular momentum, the centrifugal support of the baryons and dark matter within the virial radius is small. Indeed, whether calculated through linear theory or via *N*-body simulations, the 'spin' (which defines the ratio of the halo angular speed to that required for the halo to be entirely centrifugally supported) follows approximately a lognormal distribution with average value $\lambda_{\rm DM} = 0.035$ (Bett et al. 2007). This quantity is invariant to cosmological parameters, time, mass or environment (e.g. Barnes & Efstathiou 1987; Steinmetz & Bartelmann 1995; Cole & Lacey 1996).

As the gas collapses within the halo, the baryons can both lose and gain angular momentum between the virial radius and disc scale. If the baryons are dynamically cold, they fall inwards, weakly conserving specific angular momentum. Although the spin of the baryon at the virial radius is small, by the time they reach ∼2–10 kpc (the 'size' of a disc), they form a centrifugally supported disc that follows an exponential mass profile (e.g. Fall 1983; Mo, Mao & White 1998). Here, 'weakly conserved' is within a factor of 2, and indeed, observational studies suggest that late-type spiral discs have a spin of $\lambda'_{\rm disc} = 0.025$ (e.g. Courteau 1997), suggesting that only ∼ 30 per cent of the initial baryonic angular momentum is lost due to viscous angular momentum redistribution and selective gas losses that occur as the galaxy discs forms (e.g. Burkert 2009).

In contrast, if the baryons do not make it into the disc, they are redistributed (e.g. due to mergers), or blown out of the galaxy due to winds, then the spin of the disc is much lower than that of the halo. Indeed, the fraction of the initial halo angular momentum that is lost must be as high as ∼ 90 per cent for early-type and elliptical galaxies (at the same stellar mass as spirals; Bertola & Capaccioli 1975), with Sa and S0 galaxies in between the extremes of late-type spiral and elliptical galaxies (e.g. Romanowsky & Fall 2012).

Numerical models have suggested that most of the angular momentum transfer occurs at epochs earlier than $z \sim 1$, after which the baryonic discs gain sufficient angular momentum to stabilize themselves (Dekel, Sari & Ceverino 2009; Ceverino, Dekel & Bournaud 2010; Obreschkow et al. 2015; Lagos et al. 2017). For example, Danovich et al. (2015) identify four dominant phases of angular momentum exchange that dominate this process: linear tidal torques on the gas beyond and through the virial radius, angular momentum transport through the halo, dissipation and disc instabilities, and outflows in the disc itself. These processes can increase and decrease the specific angular momentum of the disc as it forms, although they eventually 'conspire' to produce discs that have a similar spin distribution as the parent dark matter halo.

Measuring the processes that control the internal redistribution of angular momentum in high-redshift discs is observationally demanding. However, on galaxy scales (i.e. ∼2–10 kpc), observations suggest redshift evolution according to $j_\star = J_\star/M_\star \propto (1+z)^n$, with $n \sim -1.5$, at least out to $z \sim 2$ (e.g. Burkert et al. 2016; Obreschkow et al. 2015). Recently, Burkert et al. (2016) exploited the KMOS^{3D} survey of $z \sim 1$–2.5 star-forming galaxies to infer the angular momentum distribution of baryonic discs, finding that their spin is broadly consistent with the dark matter haloes, with $\lambda \sim 0.037$ with a dispersion ($\sigma_{\log\lambda} \sim 0.2$). The lack of correlation between the 'spin' ($j_{\rm d}/j_{\rm DM}$) and the stellar densities of high-redshift galaxies also suggests that the redistribution of the angular momentum within the discs is the dominant process that leads to compaction (i.e. bulge formation; Burkert et al. 2016; Tadaki et al. 2017). Taken together, these results suggest that angular momentum in high-redshift discs plays a dominant role in 'crystallizing' the Hubble sequence of galaxy morphologies.

In this paper, we investigate how the angular momentum and spin of baryonic discs evolve with redshift by measuring the dynamics of a large, representative sample of star-forming galaxies between $z \sim 0.28$ and 1.65 as observed with the KMOS (*K*-band Multi-Object Spectrograph) and MUSE (Multi-Unit Spectroscopic Explorer) integral field spectrographs. We aim to measure the angular momentum of the stars and gas in large and representative samples of high-redshift galaxies. Only now, with the capabilities of sensitive, multi-deployable (or wide-area) integral field spectrographs, such as MUSE and KMOS, this is becoming possible (e.g. Bacon et al. 2015; Burkert et al. 2016; Wisnioski et al. 2015; Stott et al. 2016). We use our data to investigate how the mass, size and rotational velocity of galaxy discs evolve with cosmic time. As well as providing constraints on the processes that shape the Hubble sequence, the evolution of the angular momentum and stellar mass provides a novel approach to test galaxy formation models since these values reflect the initial conditions of their host haloes, merging and the prescriptions that describe the processes of gas accretion, star formation and feedback, all of which can strongly affect the angular momentum of the baryonic disc.

In Section 2, we describe the observations and data reduction. In Section 3, we describe the analysis used to derive stellar masses, galaxy sizes, inclinations and dynamical properties. In Section 4, we combine the stellar masses, sizes and dynamics to measure the redshift evolution of the angular momentum of galaxies. We also compare our results to hydrodynamical simulations. In Section 5, we give our conclusions. Throughout the paper, we use a cosmology with $\Omega_\Lambda = 0.73$, $\Omega_{\rm m} = 0.27$ and $H_0 = 72$ km s^{-1} Mpc^{-1}. In this cosmology, a spatial resolution of 0.7 arcsec corresponds to a physical scale of 5.2 kpc at $z = 0.84$ (the median redshift of our survey). All quoted magnitudes are on the AB system and we adopt a Chabrier initial mass function throughout.

2 OBSERVATIONS AND DATA REDUCTION

The observations for this programme were acquired from a series of programmes (commissioning, guaranteed time and open-time projects; see Table 1) with the new MUSE (Bacon et al. 2010, 2015) and KMOS (Sharples et al. 2004) on the ESO Very Large Telescope (VLT). Here, we describe the observations and data reduction, and discuss how the properties (star formation rates and stellar masses) of the galaxies in our sample compare to the 'main-sequence' population.

Table 1. Observing logs.

Field name	PID	RA (J2000)	Dec. (J2000)	t_{exp} (ks)	Seeing (arcsec)	3σ SB limit
MUSE:						
J0210−0555	060.A-9302	02:10:39.43	−05:56:41.28	9.9	1.08	9.1
J0224−0002	094.A-0141	02:24:35.10	−00:02:16.00	14.4	0.70	11.0
J0958+1202	094.A-0280	09:58:52.34	+12:02:45.00	11.2	0.80	15.2
COSMOS-M1	060.A-9100	10:00:44.26	+02:07:56.91	17.0	0.90	5.3
COSMOS-M2	060.A-9100	10:01:10.57	+02:04:10.60	12.6	1.0	6.3
TN J1338	060.A-9318	13:38:25.28	−19:42:34.56	32.0	0.75	4.1
J1616+0459	060.A-9323	16:16:36.96	+04:59:34.30	7.0	0.90	7.6
J2031−4037	060.A-9100	20:31:54.52	−40:37:21.62	37.7	0.83	5.2
J2033−4723	060.A-9306	20:33:42.23	−47:23:43.69	7.9	0.85	7.4
J2102−3535	060.A-9331	21:02:44.97	−35:53:09.31	11.9	1.00	6.2
J2132−3353	060.A-9334	21:32:38.97	−33:53:01.72	6.5	0.70	13.6
J2139−0824	060.A-9325	21:39:11.86	−38:24:26.14	7.4	0.80	5.7
J2217+1417	060.A-9326	22:17:20.89	+14:17:57.01	8.1	0.80	4.9
J2217+0012	095.A-0570	22:17:25.01	+00:12:36.50	12.0	0.69	6.0
HDFS-M2	060.A-9338	22:32:52.71	−60:32:07.30	11.2	0.90	7.3
HDFS-M1	060.A-9100	22:32:55.54	−60:33:48.64	107.5	0.80	2.8
J2329−0301	060.A-9321	23:29:08.27	−03:01:58.80	5.7	0.80	5.6
KMOS:						
COSMOS-K1	095.A-0748	09:59:33.54	+02:18:00.43	16.2	0.70	22.5
SSA22	060.A-9460	22:19:30.45	+00:38:53.34	7.2	0.72	31.2
SSA22	060.A-9460	22:19:41.15	+00:23:16.65	7.2	0.70	33.7

Notes. RA and Dec. denote the field centres. The seeing is measured from stars in the field of view (MUSE) or from a star placed on one of the IFUs (KMOS). The units of the surface brightness limit are $\times 10^{-19}$ erg s^{-1} cm^{-2} arcsec^{-2}. The reduced MUSE data cubes for these fields are available at http://astro.dur.ac.uk/~ams/MUSEcubes/

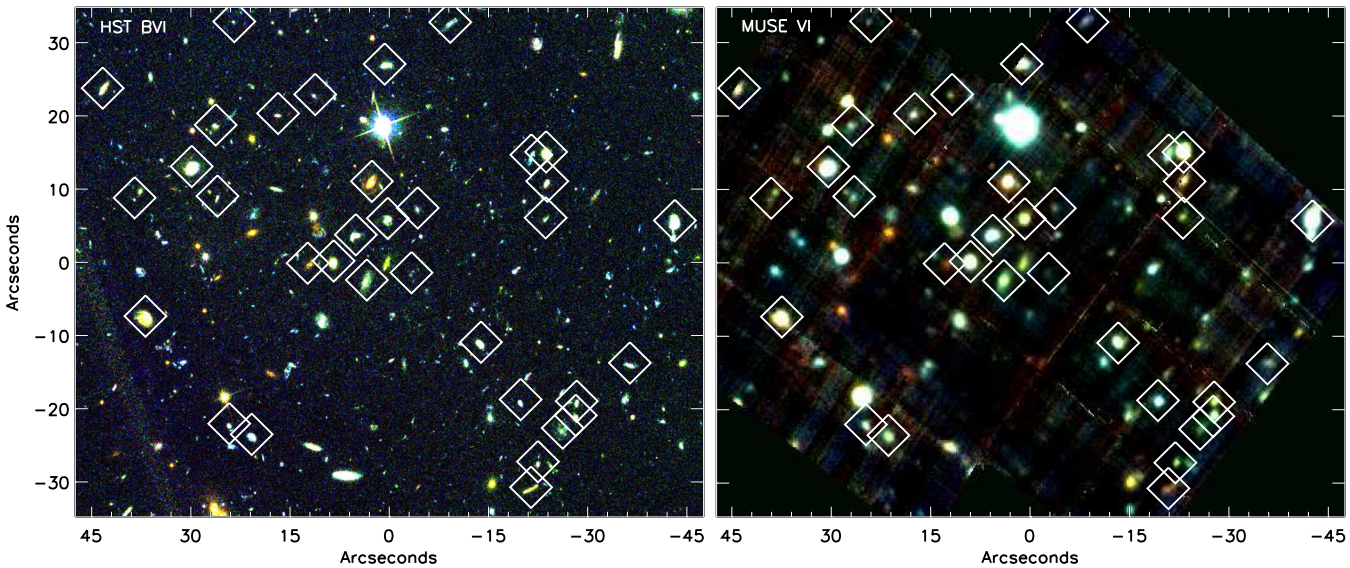

Figure 1. *HST* and MUSE images for one of our survey fields, TN J1338−13, that contains a $z = 4.4$ radio galaxy – underlining the fact that our survey of the foreground galaxy population is unbiased. Left: *HST BVI*-band colour image. The [O II] emitters identified from this field are also marked by open symbols. Centre: MUSE *VI*-band colour image of the cube generated from three equal wavelength ranges. The [O II] emitters are again marked. Each image is centred with (0,0) at α: $13^h\ 38^m\ 26\overset{s}{.}1$, δ: $-19^\circ\ 42'\ 30\overset{''}{.}5$ with north up and east left.

2.1 MUSE observations

As part of the commissioning and science verification of the MUSE spectrograph, observations of 15 'extragalactic' fields were taken between 2014 February and 2015 February. The science targets of these programmes include 'blank' field studies (e.g. observations of the Hubble Ultra-Deep Field; Bacon et al. 2015), as well as high-redshift ($z > 2$) galaxies, quasars and galaxy clusters (e.g. Fig. 1; see also Contini et al. 2016; Husband et al. 2015; Richard et al. 2015). The wavelength coverage of MUSE (4770–9300 Å in its standard configuration) allows us to serendipitously identify [O II] emitters between $z \sim 0.3$ and 1.5 in these fields and so to study the dynamics of star-forming galaxies over this redshift range. We exploit these observations to construct a sample of star-forming galaxies, selected via their [O II] emission. The programme IDs, pointing centres, exposure times and seeing full width at half-maximum (FWHM;

as measured from stars in the continuum images) for all of the MUSE pointings are given in Table 1. We also supplement these data with [O II] emitters from MUSE observations from two open-time projects (both of whose primary science goals are also to detect and resolve the properties of $z > 3$ galaxies/QSOs; Table 1). The median exposure time for each of these fields is 12 ks, but ranges from 5.4 to 107.5 ks. In total, the MUSE survey area exploited here is ∼20 arcmin^2 with a total integration time of 89 h.

The MUSE Integral Field Unit (IFU) provides full spectral coverage spanning 4770–9300 Å and a contiguous field of view of 60 arcsec × 60 arcsec, with a spatial sampling of 0.2 arcsec pixel^{-1} and a spectral resolution of $R = \lambda/\Delta\lambda = 3500$ at $\lambda = 7000$ Å (the wavelength of the [O II] at the median redshift of our sample) – sufficient to resolve the [O II] λλ3726.2,3728.9 emission line doublet. In all cases, each 1 h observing block was split into a number of sub-exposures (typically 600, 1200 or 1800 s) with small (2 arcsec) dithers between exposures to account for bad pixels. All observations were carried out in dark time, with good sky transparency. The average *V*-band seeing for the observations was 0.7 arcsec (Table 1).

To reduce the data, we use the MUSE ESOREX pipeline that extracts, wavelength calibrates and flat-fields the spectra and forms each data cube. In all of the data taken after 2014 August, each 1 h science observation was interspersed with a flat-field to improve the slice-by-slice flat-field (illumination) effects. Sky subtraction was performed on each sub-exposure by identifying and subtracting the sky emission using blank areas of sky at each wavelength slice, and the final mosaics were then constructed using an average with a 3σ clip to reject cosmic rays, using point sources in each (wavelength-collapsed) image to register the cubes. Flux calibration was carried out using observations of known standard stars at similar airmass and were taken immediately before or after the science observations. In each case, we confirmed the flux calibration by measuring the flux density of stars with known photometry in the MUSE science field.

To identify [O II] emitters in the cubes, we construct and co-add *V*- and *I*-band continuum images from each cube by collapsing the cubes over the wavelength ranges λ = 4770–7050 and 7050–9300 Å, respectively. We then use SEXTRACTOR (Bertin & Arnouts 1996) to identify all of the >4σ continuum sources in the 'detection' images. For each continuum source, we extract a 5 × 5 arcsec sub-cube (centred on each continuum source) and search both the one- and two-dimensional spectra for emission lines. At this resolution, the [O II] doublet is resolved and so trivially differentiated from other emission lines, such as Lyα, [O III] 4959,5007 or Hα+[N II] 6548,6583. In the cases where an emission line is identified, we measure the wavelength, *x*/*y* (pixel) position and RA/Dec. of the galaxy. Since we are interested in resolved dynamics, we only include galaxies where the [O II] emission line is detected above 5σ in the one-dimensional spectrum. To ensure that we do not miss any [O II] emitters that do not have continuum counterparts, we also remove all of the continuum sources from each cube by masking a 5 arcsec diameter region centred on the continuum counterpart, and search the remaining cube for [O II] emitters. We do not find any additional [O II]-emitting galaxies where the integrated [O II] flux is detected above a signal-to-noise (S/N) of 5 (i.e. all of the bright [O II] emitters in our sample have at least a 4σ detection in continuum).

In Fig. 1, we show an *HST BVI*-band colour image of one of our target fields, TN J1338, along with a colour image generated from the 32 ks MUSE exposure. The blue, green and red channels are generated from equal-width wavelength ranges between 4770 and 9300 Å, in the MUSE cube. In both panels, we identify all of the [O II] emitters. In this single field alone, there are 33 resolved [O II] emitters.

From all 17 MUSE fields considered in this analysis, we identify a total of 431 [O II] emitters with emission line fluxes ranging from 0.1 to 170 × 10^{-17} erg s^{-1} cm^{-2} with a median flux of 3 × 10^{-17} erg s^{-1} cm^{-2} and a median redshift of $z = 0.84$ (Fig. 2).

Before discussing the resolved properties of these galaxies, we first test how our [O II]-selected sample compares to other [O II] surveys at similar redshifts. We calculate the [O II] luminosity of each galaxy, and in Fig. 2 we show the [O II] luminosity function in

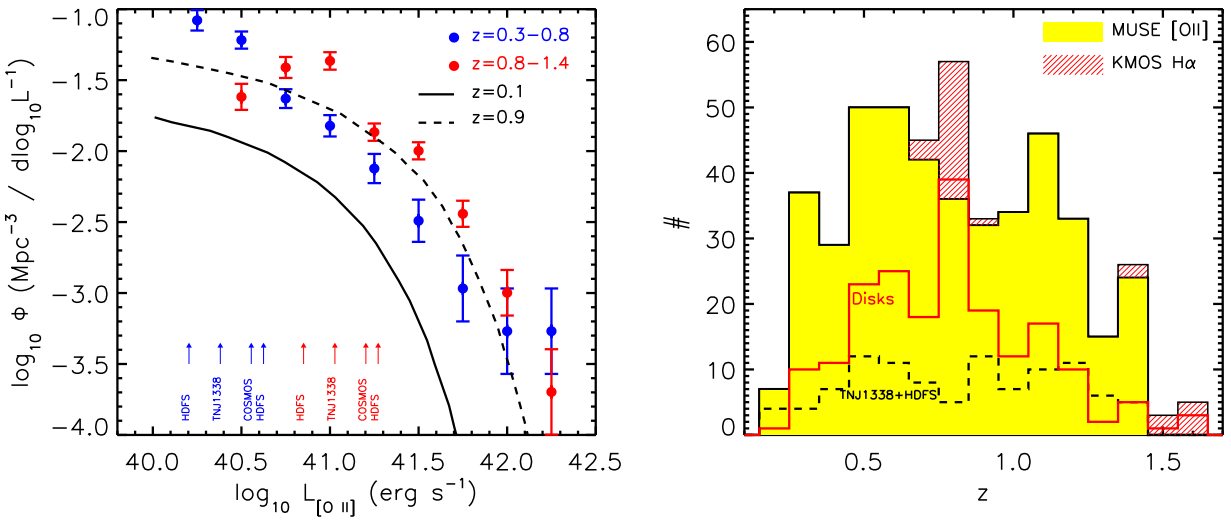

Figure 2. Left: [O II] luminosity function for the star-forming galaxies in our sample from the 18 MUSE IFU pointings. We split the sample into two redshift bins, $z = 0.3$–0.8 and 0.8–1.4. The arrows on the plot denote luminosity limits for four of the fields in the MUSE sample (which span the complete range of depths). To baseline these results, we overlay the [O II] luminosity function at $z = 0$ from SDSS (Ciardullo et al. 2013) that shows that there is strong evolution in $L^{\star}_{[OII]}$ from $z \sim 0$ to $z \sim 0.5$. This evolution is also seen in other [O II] surveys (e.g. Ly et al. 2007; Khostovan et al. 2015). Right: the redshift distribution of the [O II] and Hα emitters in our MUSE and KMOS samples. Our sample has a median redshift of $z = 0.84$ and a full redshift range of $z = 0.28$–1.67. Since the MUSE observations have a wide range of exposure times, from 5.7 to 107.5 ks, we overlay the redshift distribution of the [O II] emitters in the two deepest fields, HDFS and TN J1338, to highlight that the highest redshift galaxies are not dominated by the deepest observations. We also overlay the redshift distribution of the galaxies classified as 'rotationally supported' (i.e. discs).

two redshift bins ($z = 0.3$–0.8 and 0.8–1.4). In both redshift bins, we account for the incompleteness caused by the exposure time differences between fields. We highlight the luminosity limits for four of the fields that span the whole range of depths in our survey. This figure shows that the [O II] luminosity function evolves strongly with redshift, with $L^\star$ evolving from $\log_{10}(L^\star[\mathrm{erg\ s^{-1}\ cm^{-2}}]) = 41.06 \pm 0.17$ at $z = 0$ to $\log_{10}(L^\star[\mathrm{erg\ s^{-1}\ cm^{-2}}]) = 41.5 \pm 0.20$ and $\log_{10}(L^\star[\mathrm{erg\ s^{-1}\ cm^{-2}}]) = 41.7 \pm 0.22$ at $z = 1.4$ (see also Ly et al. 2007; Khostovan et al. 2015). The same evolution has also been seen at UV wavelengths (Oesch et al. 2010) and in Hα emission (e.g. Sobral et al. 2013a).

2.2 KMOS observations

We also include observations of the redshifted Hα in 46 $z \sim$0.8–1.7 galaxies from three well-studied extragalactic fields. Two of these fields are taken from an Hα-selected sample at $z = 0.84$ from the KMOS–Hi-z emission line survey (KMOS-HiZELS; Geach et al. 2008; Sobral et al. 2009, 2013a) and are discussed in Sobral et al. (2013b, 2015) and Stott et al. (2014). Briefly, observations of 29 Hα-selected galaxies were taken between 2013 June and 2013 July using KMOS with the *YJ*-band filter as part of the KMOS science verification programme. The near-infrared KMOS IFU comprises 24 IFUs, each of size 2.8 × 2.8 arcsec sampled at 0.2 arcsec that can be deployed across a 7 arcmin diameter patrol field. The total exposure time was 7.2 ks pixel^{-1}, and we used object–sky–object observing sequences, with one IFU from each of the three KMOS spectrographs placed on sky to monitor OH variations.

Further KMOS observations were also obtained between 2015 April 25 and April 27 as the first part of a 20 night KMOS guaranteed time programme aimed at resolving the dynamics of 300 mass-selected galaxies at $z \sim$ 1.2–1.7. 17 galaxies were selected from photometric catalogues of the COSMOS field. We initially selected targets in the redshift range $z = 1.3$–1.7 and brighter than $K_{\mathrm{AB}} = 22$ (a limit designed to ensure that we obtain sufficient S/N per resolution element to spatially resolve the galaxies; see Stott et al. 2016 for details). To ensure that the Hα emission is bright enough to detect *and* spatially resolve with KMOS, we pre-screened the targets using the Magellan Multi-object Infrared Spectrograph to search for and measure the Hα flux of each target, and then carried out follow-up observations with KMOS of those galaxies with Hα fluxes brighter than 5×10^{-17} erg s^{-1} cm^{-2}. These KMOS observations were carried out using the *H*-band filter, which has a spectral resolution of $R = \lambda/\Delta\lambda = 4000$. We used object–sky–object sequences, with one of the IFUs placed on a star to monitor the point spread function (PSF) and one IFU on blank sky to measure OH variations. The total exposure time was 16.2 ks (split into three 5.4 ks OBs, with 600 s sub-exposures). Data reduction was performed using the SPARK pipeline with additional sky subtraction and mosaicking carried out using customized routines. We note that a similar dynamical/angular momentum analysis of the ∼800 galaxies at $z \sim 1$ from the KMOS Redshift One Spectroscopic Survey (KROSS) survey will be presented in Harrison et al. (2017).

2.3 Final sample

Combining the two KMOS samples, in total there are 41/46 Hα-emitting galaxies suitable for this analysis (i.e. Hα detected above an S/N > 5 in the collapsed, one-dimensional spectrum). From our MUSE sample of 431 galaxies, 67 of the faintest [O II] emitters are only detected above an S/N = 5 when integrating a 1 × 1 arcsec region, and so no longer considered in the following analysis, leaving us with a sample of 364 [O II] emitters for which we can measure resolved dynamics. Together, the MUSE and KMOS sample used in the following analysis comprises 405 galaxies with a redshift range $z = 0.28$–1.63. We show the redshift distribution for the full sample in Fig. 2. The multiwavelength and dynamical properties of all galaxies in our sample are provided in Table 2.

3 ANALYSIS

With the sample of 405 emission line galaxies in our survey fields, the first step is to characterize the integrated properties of the galaxies. In the following, we investigate the spectral energy distributions (SEDs), stellar masses and star formation rates, sizes, dynamics and their connection with the galaxy morphology, and we put our findings in the context of our knowledge of the general galaxy population at these redshifts. We first discuss their stellar masses.

3.1 SEDs and stellar masses

The majority of the MUSE and KMOS fields in our sample have excellent supporting optical/near- and mid-infrared imaging, and so to infer the stellar masses and star formation rates for the galaxies in our sample, we construct the SEDs for each galaxy. In most cases, we exploit archival *HST*, Subaru, *Spitzer*/IRAC, United Kingdom Infrared Telescope/Wide Field Camera (WFCAM) and/or VLT/Hawk-I imaging. In the optical/near-infrared imaging, we measure 2 arcsec aperture photometry, whilst in the IRAC 3.6/4.5 μm bands we use 5 arcsec apertures (and apply appropriate aperture corrections based on the PSF in each case). We list all of the properties for each galaxy, and show their broad-band SEDs in Table A1. We use HYPER-z (Bolzonella, Miralles & Pelló 2000) to fit the photometry of each galaxy at the known redshift, allowing a range of star formation histories from late to early types and reddenings of $A_{\mathrm{V}} = 0$–3 in steps of $\Delta A_{\mathrm{V}} = 0.2$ and a Calzetti dust reddening curve (Calzetti et al. 2000). In cases of non-detections, we adopt a 3σ upper limit.

We show the observed photometry and overlay the best-fitting HYPER-z SED for all of the galaxies in our sample in Figs A1–A3. Using the best-fitting parameters, we then estimate the stellar mass of each galaxy by integrating the best-fitting star formation history, accounting for mass-loss according to the STARBURST99 mass-loss rates (Leitherer et al. 1999). We note that we only calculate stellar masses for galaxies that have detections in >3 wavebands, although include the best SEDs for all sources in Figs A1–A3. Using the stellar masses and rest-frame *H*-band magnitudes, we derive a median mass-to-light ratio for the full sample of $M_\star/L_{\mathrm{H}} = 0.20 \pm 0.01$. The best-fitting reddening values and the stellar masses for each galaxy are also given in Table A1.

As a consistency check that our derived stellar masses are consistent with those derived from other SED fitting codes, we compare our results with Muzzin et al. (2013) who derive the stellar masses of galaxies in the COSMOS field using the EASY photometric redshift code (Brammer, van Dokkum & Coppi 2008) with stellar mass estimated using FAST (Kriek et al. 2009). For the 54 [O II]-emitting galaxies in the COSMOS field in our sample, the stellar masses we derive are a factor of 1.19 ± 0.06 higher than those derived using FAST. Most of this difference can be attributed to degeneracies in the redshifts and best-fitting star formation histories. Indeed, if we limit the comparison to galaxies where the photometric and spectroscopic redshifts agree within $\Delta z < 0.2$, and where the luminosity-weighted ages also agree to within a factor of 1.5, then the ratio of the stellar masses from HYPER-z/EASY is 1.02 ± 0.04.

Table 2. Galaxy properties. The full table is given in the online version of this paper. The first five rows are shown here for their content.

ID	RA (J2000)	Dec.	z	V_{AB}	K_{AB}	f_{neb}	$r_{h,\star}$ (arcsec)	$r_{h,neb}$ (arcsec)	M_H	$\log(\frac{M_\star}{M_\odot})$	σ_{gal} (km s^{-1})	σ_{int} (km s^{-1})	$V(3\,R_d)$ (km s^{-1})	i	A_V	$j_\star$ (km s^{-1} kpc)	SFR ($M_\odot$ yr^{-1})	Class
COSMOS-K1-1	09:59:40.603	+02:21:04.15	1.6350	24.98	22.53	5.7	0.41 ± 0.10	0.45 ± 0.15	−22.25	10.48	131 ± 3	46 ± 3	16 ± 7	22 ± 22	0.2	66 ± 41	11	D
COSMOS-K1-2	09:59:31.589	+02:19:05.47	1.6164	23.70	20.63	5.1	0.18 ± 0.01	0.24 ± 0.05	−24.46	11.40	176 ± 3	–	–	–	0.6	345 ± 6	16	C
COSMOS-K1-3	09:59:33.994	+02:20:54.58	1.5240	23.90	21.73	5.0	0.57 ± 0.13	0.68 ± 0.13	−22.85	10.57	123 ± 3	38 ± 3	206 ± 30	37 ± 10	0.4	1171 ± 463	10	D
COSMOS-K1-4	09:59:28.339	+02:19:50.53	1.4855	21.02	19.96	86.9	0.08 ± 0.05	0.30 ± 0.26	−24.51	11.09	580 ± 3	–	–	–	0.0	–	100	I
COSMOS-K1-10	09:59:30.902	+02:18:53.04	1.5489	24.06	21.60	15.4	0.20 ± 0.02	0.04 ± 0.05	−23.21	10.72	159 ± 3	–	–	–	0.6	344 ± 5	44	C

Notes. f_{neb} denotes the nebular emission line flux ([O II] in the case of MUSE and Hα for KMOS) in units of 10^{-17} erg cm^{-2} s^{-1}. $r_{h,\star}$ and $r_{h,neb}$ are the (deconvolved) continuum and nebular emission half-light radii, respectively. σ_{neb} denotes the galaxy-integrated velocity dispersion as measured from the one-dimensional spectrum. σ_{int} denotes the average intrinsic velocity dispersion within the galaxy (after correcting for beam-smearing effects). $V(3\,R_d)$ is the observed velocity at 3 R_d. i is the disc inclination. SFR is measured from the [O II] flux with SFR = 0.8×10^{-41} $L_{[O\,II]}$ erg s^{-1} and correcting for dust reddening using the Calzetti reddening law.

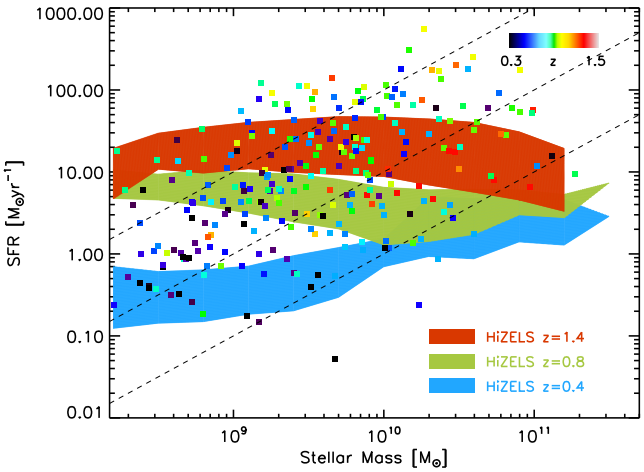

Figure 3. Star formation rate versus mass for the galaxies in our sample (with points colour-coded by redshift). As a guide, we also overlay tracks of constant specific star formation rate (sSFR) with sSFR = 0.1, 1 and 10 Gyr^{-1}. We also overlay the star formation rate–stellar mass relation at three redshift slices (z = 0.40, 0.84 and 1.47) from the Hα narrow-band selected sample from HiZELS (Sobral et al. 2013a). This shows that although the galaxies in our MUSE and KMOS samples span a wide range of stellar mass and star formation rate, they are comparable to the general field population, with specific star formation rates of sSFR ∼ 0.1–10 Gyr^{-1}.

To place the galaxies we have identified in the MUSE and KMOS data in the context of the general population at their respective redshifts, next we calculate their star formation rates (and specific star formation rates). We first calculate the [O II] or Hα emission luminosity ($L_{[OII]}$ and $L_{H\alpha}$, respectively). To account for dust obscuration, we adopt the best-fitting stellar reddening (A_V) from the stellar SED returned by HYPER-z and convert this to the attenuation at the wavelength of interest ($A_{[OII]}$ or $A_{H\alpha}$) using a Calzetti reddening law (Calzetti et al. 2000). Next, we assume that the gas and stellar phases are related by $A_{gas} = A_\star$ (1.9 – 0.15 $A_\star$) (Wuyts et al. 2013), and then calculate the total star formation rates using SFR = $C \times 10^{-42}$ $L_{[O\,II]}$ $10^{0.4A_{gas}}$, with C = 0.82 and 4.6 for the [O II] and Hα emitters, respectively. The star formation rates of the galaxies in our sample range from 0.1 to 300 M$_\odot$ yr^{-1}. In Fig. 3, we plot the specific star formation rate (sSFR = SFR/$M_\star$) versus stellar mass for the galaxies in our sample. This also shows that our sample displays a wide range of stellar masses and star formation rates, with median and quartile ranges of $\log_{10}(M_\star/M_\odot) = 9.4 \pm 0.9$ and SFR = $4.7^{+2.2}_{-2.5}$ M$_\odot$ yr^{-1}. As a guide, in this plot, we also overlay a track of constant star formation rate with SFR = 1 M$_\odot$ yr^{-1}. To compare our galaxies to the high-redshift star-forming population, we also overlay the specific star formation rate for ∼2500 galaxies from the HiZELS survey that selects Hα-emitting galaxies in three narrow redshift slices at z = 0.40, 0.84 and 1.47 (Sobral et al. 2013a). For this comparison, we calculate the star formation rates for the HiZELS galaxies in an identical manner to that for our MUSE and KMOS sample. This figure shows that the median specific star formation rates of the galaxies in our MUSE and KMOS samples appear to be consistent with the so-called main sequence of star-forming galaxies at their appropriate redshifts.

3.2 Galaxy sizes and size evolution

Next, we turn to the sizes for the galaxies in our sample. Studies of galaxy morphology and size, particularly from observations

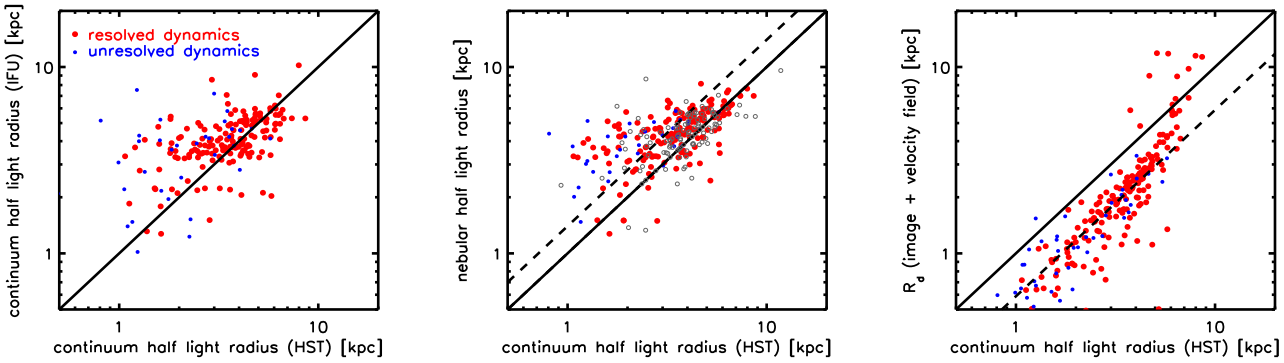

Figure 4. Comparison of the physical half-light radii of the galaxies in our sample as measured from *HST* and MUSE/KMOS imaging. Left: continuum half-light radii as measured from *HST* broad-band imaging compared to those measured from the MUSE continuum image. Large red points denote sources that are resolved by MUSE or KMOS. Small blue points denote galaxies that are unresolved (or compact) in the MUSE or KMOS data. The median ratio of the half-light radii is $r_{\rm HST}/r_{\rm MUSE} = 0.97 \pm 0.03$ (including unresolved sources and deconvolved for seeing). Centre: continuum half-light radius from *HST* versus nebular emission half-light radius (MUSE and KMOS) for the galaxies in our sample from MUSE and KMOS. The continuum and nebular emission line half-light radii are well correlated, although the nebular emission line half-light radii are systematically larger than the continuum sizes, with $r_{\rm [OII]}/r_{\rm HST} = 1.18 \pm 0.03$ (see also Nelson et al. 2016). Although not included in the fit, we also include on the plot the continuum size measurements from MUSE and KMOS as small grey points. These increase the scatter (as expected from the data in the left-hand panel), although the median ratio of nebular emission to continuum size is unaffected if these points are included. Right: comparison of the disc scalelength (measured from the dynamical modelling) versus the continuum half-light radius from *HST*. The median ratio of the half-light radius is larger than the disc radius by a factor $r_{\rm HST}/R_{\rm d} = 1.70 \pm 0.05$, which is consistent with that expected for an exponential disc.

made with *HST*, have shown that the physical sizes of galaxies increase with cosmic time (e.g. Giavalisco, Steidel & Macchetto 1996; Ferguson et al. 2004; Oesch et al. 2010). Indeed, late-type galaxies have continuum (stellar) half-light radii that are on average a factor of ∼1.5 smaller at $z \sim 1$ than at the present day (Morishita, Ichikawa & Kajisawa 2014; van der Wel et al. 2014). As one of the primary aims of this study is to investigate the angular momentum of the galaxy discs, the continuum sizes are an important quantity.

We calculate the half-light radii in both continuum and emission lines for all galaxies in our sample. Approximately 60 per cent of the galaxies in our sample have been observed with *HST* (using Advanced Camera for Surveys (ACS)/*BVI* and/or Wide Field Camera 3 (WFC3)/*JH*-band imaging). Since we are interested in the extent of the stellar light, we measure the half-light radius for each galaxy in the longest wavelength image available (usually ACS *I* or WFC *H* band). To measure the half-light radius of each galaxy, we first fit a two-dimensional Sérsic profile to the galaxy image to define an *x*/*y* centre and ellipticity for the galaxy, and then measure the total flux within 1.5 × Petrosian radius and use the curve of growth (growing ellipses from zero to 1.5 × Petrosian aperture) to measure the half-light radius. A significant fraction of our sample do not have observations with *HST* and so we also construct continuum images from the IFU data cubes and measure the continuum size in the same way (deconvolving for the PSF). In Fig. 4, we compare the half-light radius of the galaxies in our sample from *HST* observations with that measured from the MUSE and KMOS continuum images. From this, we derive a median ratio of $r_{1/2,\rm HST}/r_{1/2,\rm MUSE} = 0.97 \pm 0.03$ with a scatter of 30 per cent (including unresolved sources in both cases).

For each galaxy in our sample, we also construct a continuum-subtracted narrow-band [O II] or Hα emission line image (using 200 Å on either size of the emission line to define the continuum) and use the same technique to measure the half-light radius of the nebular emission. The continuum and nebular emission line half-light radii (and their errors) for each galaxy are given in Table A1. As Fig. 4 shows, the nebular emission is more extended than the continuum with $r_{1/2,\rm [OII]}/r_{1/2,\rm HST} = 1.18 \pm 0.03$. This is consistent with recent results from the 3D *HST* survey that demonstrates that the nebular emission from $\sim L^{\star}$ galaxies at $z \sim 1$ tends to be systematically more extended than the stellar continuum (with weak dependence on mass; Nelson et al. 2016).

We also compare the continuum half-light radius with the disc scalelength, $R_{\rm d}$ (see Section 3.4). From the data, we measure $r_{1/2,\,\rm HST}/R_{\rm d} = 1.70 \pm 0.05$. For a galaxy with an exponential light profile, the half-light radii and disc scalelength are related by $r_{1/2} = 1.68\,R_{\rm d}$, which is consistent with our measurements (and we overlay this relation in Fig. 4). In Fig. 5, we plot the evolution of the half-light radii (in kpc) of the nebular emission with redshift for the galaxies in our sample that shows that the nebular emission half-light radii are consistent with similar recent measurements of galaxy sizes from *HST* (Nelson et al. 2016), and a factor of ∼1.5 smaller than late-type galaxies at $z = 0$.

From the full sample of [O II] or Hα emitters, the spatial extent of the nebular emission of 75 per cent of the sample is spatially resolved beyond the seeing, with little/no dependence on redshift, although the unresolved sources unsurprisingly tend to have lower stellar masses (median $M_{\star}^{\rm unresolved} = 1.0 \pm 0.5 \times 10^9$ M$_{\odot}$ compared to median $M_{\star}^{\rm resolved} = 3 \pm 1 \times 10^9$ M$_{\odot}$).

3.3 Resolved dynamics

Next, we derive the velocity fields and line-of-sight velocity dispersion maps for the galaxies in our sample. The two-dimensional dynamics are critical for our analysis since the circular velocity, which we will use to determine the angular momentum in Section 4, must be taken from the rotation curve at a scale radius. The observed circular velocity of the galaxy also depends on the disc inclination, which can be determined using either the imaging or dynamics, or both.

To create intensity, velocity and velocity dispersion maps for each galaxy in our MUSE sample, we first extract a 5 × 5 arcsec 'sub-cube' around each galaxy (this is increased to 7 × 7 arcsec if the [O II] is very extended) and then fit the [O II] emission line doublet

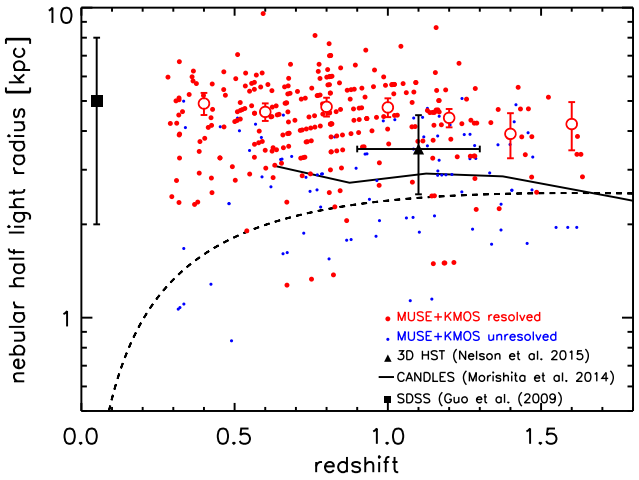

Figure 5. Evolution of the physical half-light radii with redshift for the galaxies in our sample. We plot the nebular emission line sizes in all cases ([O II] for MUSE or Hα for KMOS). We plot both the extended (red) and unresolved/compact (blue) galaxies individually, but also show the median half-light radii in $\Delta z = 0.2$ bins as large filled points with errors (these medians include unresolved sources). We also include recent measurements of the nebular emission line half-light radii of $z \sim 1$ galaxies from the 3D *HST* survey (Nelson et al. 2016) and the evolution in the continuum sizes (corrected to nebular sizes using the results from Fig. 4) from Morishita et al. (2014) for galaxies in the CANDLES fields. We also include the size measurements from SDSS (Guo et al. 2009). As a guide, the dashed line shows the half-light radius as a function of redshift for a 0.7 arcsec PSF (the median seeing of our observations). This plot shows that the nebular emission half-light radii of the galaxies in our sample are consistent with similar recent measurements of galaxy sizes from *HST* (Nelson et al. 2016), and a factor of $\sim$1.5 smaller than late-type galaxies at $z = 0$.

pixel by pixel. We first average over 0.6 × 0.6 arcsec pixels and attempt the fit to the continuum plus emission lines. During the fitting procedure, we account for the increased noise around the sky OH residuals, and also account for the spectral resolution (and spectral line spread function) when deriving the line width. We only accept the fit if the improvement over a continuum-only fit is $>5\sigma$. If no fit is achieved, the region size is increased to 0.8 × 0.8 arcsec and the fit re-attempted. In each case, the continuum level, redshift, line width and intensity ratio of the 3726.2/3728.9 Å [O II] emission line doublet are allowed to vary. In cases that meet the S/N threshold, errors are calculated by perturbing each parameter in turn, allowing the other parameters to find their new minimum, until a $\Delta\chi^2 = 1\sigma$ is reached. For the KMOS observations, we follow the same procedure, but fit the Hα and [N II] 6548,6583 emission lines. In Fig. 6, we show example images and velocity fields for the galaxies in our sample (the full sample along with their spectra are shown in Appendix A (see online)). In Fig. 6, the first three panels show the *HST* image, with ellipses denoting the disc radius and lines identifying the major morphological and kinematic axis (see Section 3.4), the MUSE *I*-band continuum image and the two-dimensional velocity field. We note that for each galaxy, the high-resolution image (usually from *HST*) is astrometrically aligned to the MUSE or KMOS cube by cross-correlating the (line-free) continuum image from the cube.

The ratio of circular velocity (or maximum velocity if the dynamics are not regular) to line-of-sight velocity dispersion (V/σ) provides a crude, but common way to classify the dynamics of galaxies into rotationally versus dispersion-dominated systems. To estimate the maximum circular velocity, V, we extract the velocity profile through the continuum centre at a position angle that maximizes the velocity gradient. We inclination correct this value using the continuum axis ratio from the broad-band continuum morphology (see Section 3.4). For the full sample, we find a range of maximum velocity gradients from 10 to 540 km s^{-1} (peak to peak) with a median of 98 ± 5 km s^{-1} and a quartile range of 48–192 km s^{-1}. To estimate the intrinsic velocity dispersion, we first remove the effects of beam smearing (an effect in which the observed velocity dispersion in a pixel has a contribution from the intrinsic dispersion and the flux-weighted velocity gradient across that pixel due to the PSF). To derive the intrinsic velocity dispersion, we calculate and subtract the luminosity-weighted velocity gradient across each pixel and then calculate the average velocity dispersion from the corrected two-dimensional velocity dispersion map. In this calculation, we omit pixels that lie within the central PSF FWHM (typically $\sim$0.6 arcsec; since this is the region of the galaxy where the beam-smearing correction is most uncertain). For our sample, the average (corrected) line-of-sight velocity dispersion is $\sigma = 32 \pm 4$ km s^{-1} (in comparison, the average velocity dispersion measured from the galaxy-integrated one-dimensional spectrum is $\sigma = 70 \pm 5$ km s^{-1}). This average intrinsic velocity dispersion at the median redshift of our sample ($z = 0.84$) is consistent with the average velocity dispersion seen in a number of other high-redshift samples (e.g. Förster Schreiber et al. 2009; Law et al. 2009; Gnerucci et al. 2011; Epinat et al. 2012; Wisnioski et al. 2015).

For the full sample of galaxies in our survey, we derive a median inclination-corrected ratio of $V/\sigma = 2.2 \pm 0.2$ with a range of $V/\sigma = 0.1$–10 (where we use the limits on the circular velocities for galaxies classed as unresolved or irregular/face-on). We show the full distribution in Fig. 7.

Although the ratio of V/σ provides a means to separate 'rotationally dominated' galaxies from those that are dispersion supported, interacting or merging can also be classed as rotationally supported. Based on the two-dimensional velocity field, morphology and velocity dispersion maps, we also provide a classification of each galaxy into four broad groups (although in the following dynamical plots, we highlight the galaxies by V/σ and their classification).

(i) *Rotationally supported*: for those galaxies whose dynamics appear regular (i.e. a spider-line pattern in the velocity field, the line-of-sight velocity dispersion peaks near the dynamical centre of the galaxy and the rotation curve rises smoothly), we classify as rotationally supported (or 'Discs'). We further sub-divide this sample into two subsets: those galaxies with the highest quality rotation curves ($q = 1$; i.e. the rotation curve appears to flatten or turn over) and those whose rotation curves do not appear to have asymptoted at the maximum radius determined by the data ($q = 2$). This provides an important distinction since for a number of $q = 2$ cases the asymptotic rotation speed must be extrapolated (see Section 3.6). The images, spectra, dynamics and broad-band SEDs for these galaxies are shown in Fig. A1.

(ii) *Irregular*: a number of galaxies are clearly resolved beyond the seeing, but display complex velocity fields and morphologies, and so we classify them as 'Irregular'. In many of these cases, the morphology appears disturbed (possibly late-stage minor/major mergers) and/or we appear to be observing systems (close-to) face-on (i.e. the system is spatially extended as there is little/no velocity structure discernable above the errors). The images, spectra, dynamics and broad-band SEDs for these galaxies are shown in Fig. A2.

(iii) *Unresolved*: as discussed in Section 3.2, the nebular emission in a significant fraction of our sample appears unresolved (or

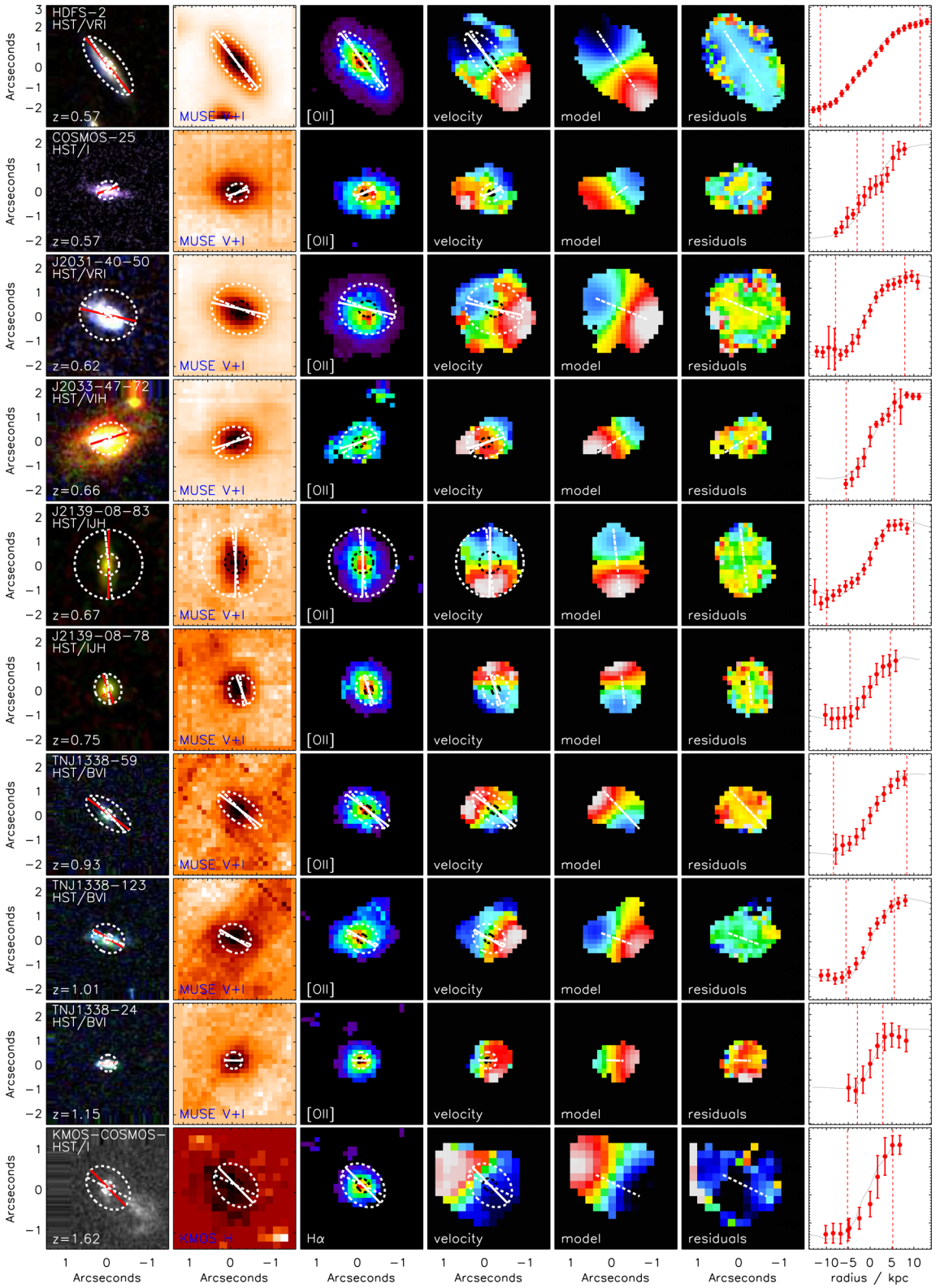

Figure 6. Example images and dynamics of nine galaxies in our sample. (a) *HST* colour image of each galaxy. given in each sub-image. The galaxies are ranked by increasing redshift. The ellipses denote the disc radius (inner ellipse R_d; outer ellipse 3 R_d). The cross denotes the dynamical centre of the galaxy and the white dashed and solid red lines show the major morphological and kinematic axes, respectively. (b) The continuum image from the IFU observations (dark scale denotes high intensity). The dashed lines are the same as in the first panel. (c) Nebular emission line velocity field. Dashed ellipses again show the disc radius at R_d and 3 R_d (the colour scale is set by the range shown in the final panel). (d) Best-fitting two-dimensional dynamical model for each galaxy. In this panel, the cross and dashed line denote the dynamical centre and major kinematic axis from our dynamical modelling. Residuals (data − model) are shown in panel (e) on the same velocity scale as the velocity and best-fitting model. The final panel shows the one-dimensional rotation curve, extracted along the major kinematic axis with a pseudo-slit of width 0.5 × FWHM of the seeing disc.

'compact') at our spatial resolution. The images, spectra, dynamics and broad-band SEDs for these galaxies are shown in Fig. A3.

(iv) *Major mergers*: Finally, a number of systems appear to comprise of two (or more) interacting galaxies on scales separated by 8–30 kpc, and we classify these as (early-stage) major mergers. The images, spectra, dynamics and broad-band SEDs for these galaxies are shown in Fig. A2.

From this broad classification, our [O II]- and Hα-selected sample comprises 24 $\pm$ 3 per cent unresolved systems, 49 $\pm$ 4 per cent rotationally supported systems (27 and 21 per cent with $q = 1$ and 2, respectively), 22 $\pm$ 2 per cent irregular (or face-on) and $\sim 5 \pm 2$ per cent major mergers. Our estimate of the 'disc' fraction in this sample is consistent with other dynamical studies over a similar redshift range that found that rotationally supported systems make up ~40–70 per cent of the Hα- or [O II]-selected star-forming population (e.g. Puech et al. 2008; Förster Schreiber et al. 2009; Epinat et al. 2012; Sobral et al. 2013b; Contini et al. 2016; Wisnioski et al. 2015; Stott et al. 2016).

From this classification, the 'rotationally supported' systems are (unsurprisingly) dominated by galaxies with high V/σ, with 176/195 (90 per cent) of the galaxies classed as rotationally supported with $V/\sigma > 1$ [and 132/195 (67 per cent) with $V/\sigma > 2$]. Concentrating only on those galaxies that are classified as rotationally supported systems (Section 3.3), we derive $V/\sigma = 2.9 \pm 0.2$ [3.4 ± 0.2 and 1.9 ± 0.2 for the $q = 1$ and 2 sub-samples, respectively]. We note that 23 per cent of the galaxies that are classified as rotationally supported have $V/\sigma < 1$ (21 per cent with $q = 1$ and 24 per cent with $q = 2$).

3.4 Dynamical modelling

For each galaxy, we model the broad-band continuum image and two-dimensional velocity field with a disc + halo model. In addition to the stellar and gaseous discs, the rotation curves of local spiral galaxies imply the presence of a dark matter halo, and so the velocity field can be characterized by

$$v^2 = v_{\rm d}^2 + v_{\rm h}^2 + v_{\rm HI}^2,$$

where the subscripts denote the contribution of the baryonic disc (stars + H_2), dark halo and extended H I gas disc, respectively. For the disc, we assume that the baryonic surface mass density follows an exponential profile (Freeman 1970)

$$\Sigma_{\rm d}(r) = \frac{M_{\rm d}}{2\pi R_{\rm d}^2} {\rm e}^{-r/R_{\rm d}},$$

where $M_{\rm d}$ and $R_{\rm d}$ are the disc mass and disc scalelength, respectively. The contribution of this disc to the circular velocity is

$$v_{\rm D}^2(x) = \frac{1}{2}\frac{GM_{\rm d}}{R_{\rm d}} (3.2\,x)^2 (I_0K_0 - I_1K_1),$$

where $x = R/R_{\rm d}$ and I_n and K_n are the modified Bessel functions computed at 1.6 x. For the dark matter component, we assume

$$v_{\rm h}^2(r) = GM_{\rm h}(<r)/r$$

with

$$\rho(r) = \frac{\rho_0\, r_0^3}{(r + r_0)\,(r^2 + r_0^2)}$$

(Persic & Salucci 1988; Burkert 1995; Salucci & Burkert 2000) where r_0 is the core radius and ρ_0 the effective core density. It follows that

$$M_{\rm h}(r) = 4\,M_0 \left[\ln\left(1 + \frac{r}{r_0}\right) - \tan^{-1}\left(\frac{r}{r_0}\right) + \frac{1}{2}\ln\left(1 + \frac{r^2}{r_0^2}\right)\right]$$

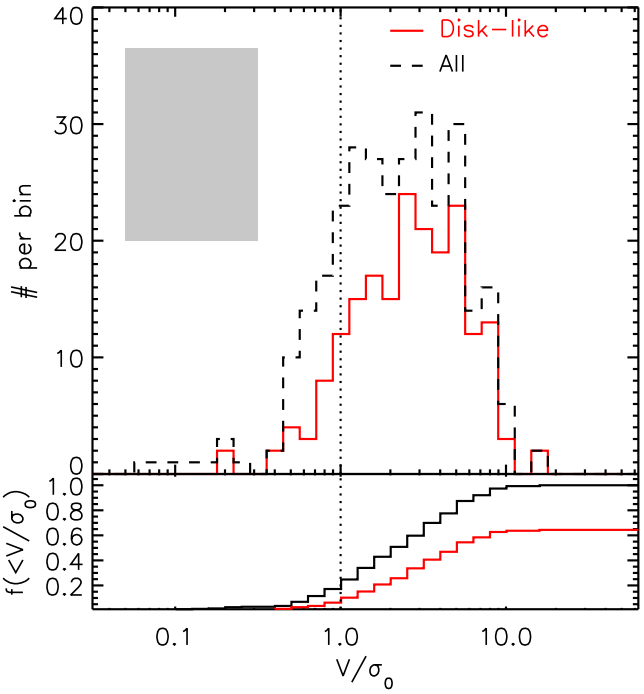

Figure 7. The ratio of circular velocity to velocity dispersion for the galaxies in our sample (V/σ), split by their classification (the lower panel shows the cumulative distribution). The circular velocity has been inclination corrected, and the velocity dispersion has been corrected for beam-smearing effects. The dashed line shows all of the galaxies in our sample that are spatially resolved. The red solid line denotes galaxies that are classified as disc-like. The grey box denotes the area occupied by the galaxies that are classified as unresolved. Finally, the dotted line shows a ratio of $V/\sigma = 1$. 90 per cent of the galaxies that are classified as disc-like (i.e. a spider-line pattern in the velocity field, the line-of-sight velocity dispersion peaks near the dynamical centre of the galaxy and the rotation curve rises smoothly) have $V/\sigma > 1$, and 67 per cent have $V/\sigma > 2$.

with $M_0 = 1.6\,\rho_0\, r_0^3$ and

$$v_H^2(r) = \frac{6.4\,G\,\rho_0\, r_0^3}{r}\left\{\ln\left(1 + \frac{r}{r_0}\right) - \tan^{-1}\left(\frac{r}{r_0}\right) + \frac{1}{2}\ln\left[1 + \left(\frac{r}{r_0}\right)^2\right]\right\}.$$

This velocity profile is generic: it allows a distribution with a core of size r_0, converges to the NFW profile (Navarro, Frenk & White 1997) at large distances and, for suitable values of r_0, it can mimic the NFW or an isothermal profile over the limited region of the galaxy that is mapped by the rotation curve.

In luminous local disc galaxies, the H I disc is the dominant baryonic component for $r > 3R_{\rm d}$. However, at smaller radii, the H I gas disc is negligible, with the dominant component in stars. Although we cannot exclude the possibility that some fraction of H I is distributed within 3 $R_{\rm d}$ and so contributes to the rotation curve, for simplicity, here we assume that the fraction of H I is small and so set $v_{\rm HI} = 0$.

To fit the dynamical models to the observed images and velocity fields, we use a Markov Chain Monte Carlo (MCMC) algorithm. We first use the imaging data to estimate of the size, position angle and inclination of the galaxy disc. Using the highest resolution image, we fit the galaxy image with a disc model, treating the [$x_{\rm im}$, $y_{\rm im}$] centre, position angle ($PA_{\rm im}$), disc scalelength ($R_{\rm d}$) and total flux as free parameters. We then use the best-fitting parameter values from the imaging as the first set of prior inputs to the code and

simultaneously fit the imaging + velocity field using the model described above. For the dynamics, the mass model has five free parameters: the disc mass ($M_{\rm d}$), radius ($R_{\rm d}$), inclination (i), the core radius r_0 and the central core density ρ_0. We allow the dynamical centre of the disc ($[x_{\rm dyn}, y_{\rm dyn}]$) and position angle ($\rm PA_{dyn}$) to vary, but require that the imaging and dynamical centre lie within 1 kpc (approximately the radius of a bulge at $z \sim 1$; Bruce et al. 2014). We also note that we allow the morphological and dynamical major axes to be independent (but see Section 3.5).

To test whether the parameter values returned by the disc modelling provide a reasonably description of the data, we perform a number of checks, in particular to test the reliability of recovering the dynamical centre, position angle and disc inclination (since these propagate directly into the extraction of the rotation curve and hence our estimate of the angular momentum).

First, we attempt to recover the parameters from a set of idealized images and velocity fields constructed from a set of realistic disc and halo masses, sizes, dynamical centres, inclinations and position angles. For each of these models, we construct a data cube from the velocity field, add noise appropriate for our observations and then re-fit the data cube to derive an 'observed' velocity field. We then fit the image and velocity field simultaneously to derive the output parameters. Only allowing the inclination to vary [i.e. fixing ($M_{\rm d}$, $R_{\rm d}$, ρ_0, r_0, $x_{\rm c}$, $y_{\rm c}$, PA) at their input values], we recover the inclinations, with $i^{\rm in} = i^{\rm out} \pm 2^{\circ}$. Allowing a completely unconstrained fit returns inclinations that are higher than the input values, ($i^{\rm in}/i^{\rm out} = 1.2 \pm 0.1$), the scatter in which can be attributed to degeneracies with other parameters. For example, the disc masses and disc sizes are overestimated (compared to the input model), with $M_{\rm d}^{\rm in}/M_{\rm d}^{\rm out} = 0.86 \pm 0.12$ and $R_{\rm d}^{\rm in}/R_{\rm d}^{\rm out} = 0.81 \pm 0.05$, but the position angle of the major axis of the galaxy is recovered to within 1° ($\rm PA_{in} - PA_{out} = 0\overset{\circ}{.}9 \pm 0\overset{\circ}{.}7$). For the purposes of this paper, since we are primarily interested in identifying the major kinematic axis (the on-sky position angle), extracting a rotation curve about this axis and correcting for inclination effects, the results of the dynamical modelling appear as sufficiently robust that meaningful measurements can be made.

Next, we test whether the inclinations derived from the morphologies alone are comparable to those derived from a simultaneous fit to the images and galaxy dynamics. To obtain an estimate of the inclination, we use GALFIT (Peng et al. 2002) to model the morphologies for all of the galaxies in our sample that have *HST* imaging. The ellipticity of the projected image is related to the inclination angle through $\cos^2 i = ((b/a)^2 - q_0^2)/(1 - q_0)^2$, where a and b are the semi-major and semi-minor axis, respectively (here i is the inclination angle of the disc plane to the plane of the sky and $i = 0$ represents an edge-on galaxy). The value of q_0 (which accounts for the fact that the discs are not thin) depends on galaxy type, but is typically in the range $q_0 = 0.13$–0.20 for rotationally supported galaxies at $z \sim 0$, and so we adopt $q_0 = 0.13$. We first construct the PSF for each *HST* field using non-saturated stars in the field of view, and then run GALFIT with Sérsic index allowed to vary from $n = 0.5$ to 7 and free centres and effective radii. For galaxies whose dynamics resemble rotating systems (such that a reasonable estimate of the inclination can be derived), the inclination derived from the morphology is strongly correlated with that inferred from the dynamics, with a median offset of just $\Delta i = 4^{\circ}$ with a spread of $\sigma_i = 12^{\circ}$.

The images, velocity fields, best-fitting kinematic maps and velocity residuals for each galaxy in our sample are shown in Figs A1–A3, and the best-fitting parameters given in Table A1. Here, the errors reflect the range of acceptable models from *all* of the models attempted. All galaxies show small-scale deviations from the best-fitting model, as indicated by the typical rms, $\langle \rm data - model \rangle = 28 \pm 5$ km s^{-1}. These offsets could be caused by the effects of gravitational instability, or simply be due to the unrelaxed dynamical state indicated by the high velocity dispersions in many cases. The goodness of fit and small-scale deviations from the best-fitting models are similar to those seen in other dynamical surveys of galaxies at similar redshifts, such as KMOS$^{\rm 3D}$ and KROSS (Wisnioski et al. 2015; Stott et al. 2016) where rotational support is also seen in the majority of the galaxies (and with rms of 10–80 km s^{-1} between the velocity field and best-fitting disc models).

3.5 Kinematic versus morphological position angle

One of the free parameters during the modelling is the offset between the major morphological axis and the major dynamical axis. The distribution of misalignments may be attributed to physical differences between the morphology of the stars and gas, extinction differences between the rest-frame UV/optical and Hα, sub-structure (clumps, spiral arms and bars) or simply measurement errors when galaxies are almost face-on. Following Franx, Illingworth & de Zeeuw (1991, see also Wisnioski et al. 2015), we define the misalignment parameter, Φ, such that $\sin \Phi = |\sin(\rm PA_{phot} - PA_{dyn})|$, where Φ ranges from 0° to 90°. For all of the galaxies in our sample whose dynamics resemble rotationally supported systems, we derive a median 'misalignment' of $\Phi = 9\overset{\circ}{.}5 \pm 0\overset{\circ}{.}5$ ($\Phi = 10\overset{\circ}{.}1 \pm 0\overset{\circ}{.}8$ and $8\overset{\circ}{.}6 \pm 0\overset{\circ}{.}9$ for $q = 1$ and 2 sub-samples, respectively). In all of the following sections, when extracting rotation curves (or velocities from the two-dimensional velocity field), we use the position angle returned from the dynamical modelling, but note that using the morphological position angle instead would reduce the peak-to-peak velocity by $\lesssim$5 per cent, although this would have no qualitative effect on our final conclusions.

3.6 Velocity measurements

To investigate the various velocity–stellar mass and angular momentum scaling relations, we require determination of the circular velocity. For this analysis, we use the best-fitting dynamical models for each galaxy to make a number of velocity measurements. We measure the velocity at the 'optical radius', $V(3\ R_{\rm d})$ (Salucci & Burkert 2000, where the half-light and disc radius are related by $r_{1/2} = 1.68\ R_{\rm d}$). Although we are using the dynamical models to derive the velocities (to reduce errors in interpolating the rotation curve data points), we note that the average velocity offset between the data and model for the rotationally supported systems at $r_{1/2}$ is small, $\Delta V = 2.1 \pm 0.5$ and 2.4 ± 1.2 km s^{-1} at $3\ R_{\rm d}$. In 30 per cent of the cases, the velocities at $3\ R_{\rm d}$ are extrapolated beyond the extent of the observable rotation curve, although the difference between the velocity of the last data point on the rotation curve and the velocity at $3\ R_{\rm d}$ in this sub-sample is only $\Delta v = 2 \pm 1$ km s^{-1} on average.

3.7 Angular momentum

With measurements of (inclination-corrected) circular velocity, size and stellar mass of the galaxies in our sample, we are in a position to combine these results and so measure the specific angular momentum of the galaxies (measuring the specific angular momentum

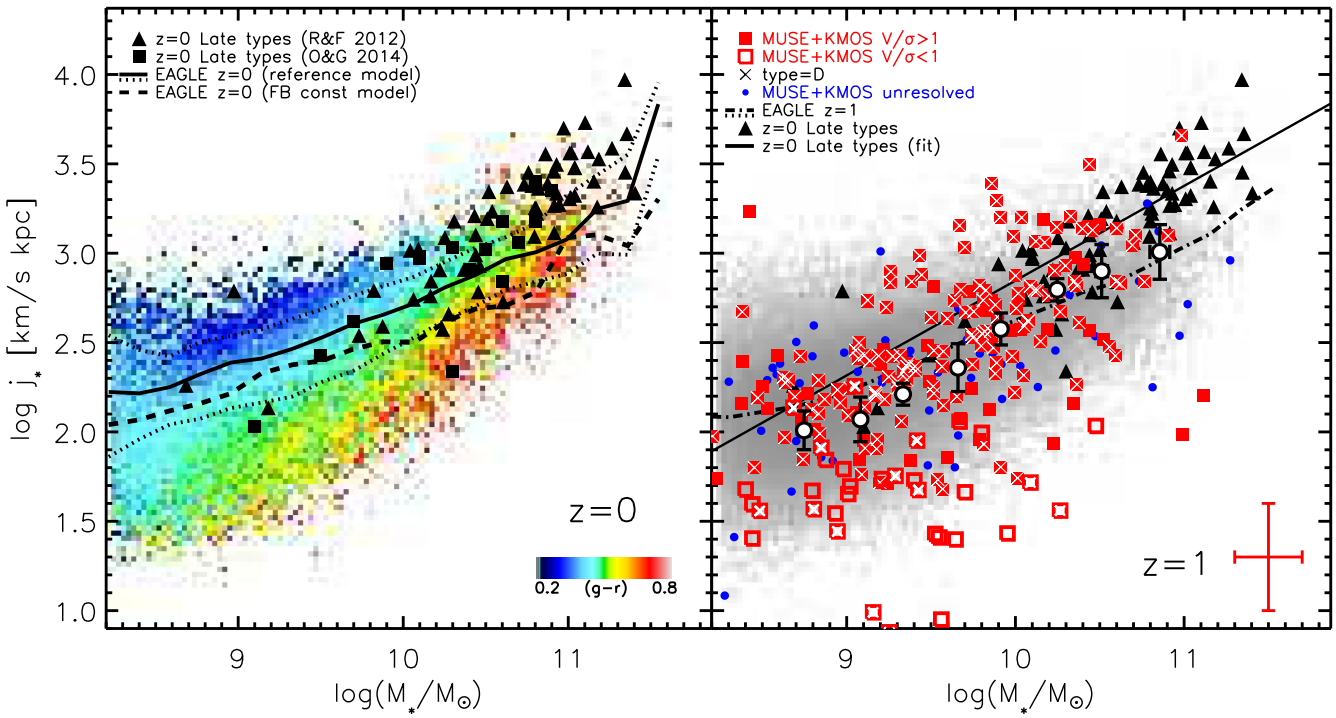

Figure 8. Left: specific angular momentum ($j_\star = J/M_\star$) of late- and early-type galaxies at $z = 0$ from Romanowsky & Fall (2012) and Obreschkow & Glazebrook (2014, R&F 2012 and O&G 2014, respectively), both of which follow a scaling of $j_\star \propto M_\star^{2/3}$. We also show the specific angular momentum of galaxies at $z = 0$ from the EAGLE simulation (reference model) with the colour scale set by the rest-frame $g - r$ colours of the galaxies. The solid line shows the median (and dotted lines denote the 68 per cent distribution width) of the EAGLE galaxies. For comparison with other EAGLE models, we also include the evolution of $j_\star$–$M_\star$ from the 'constant feedback' *FBconst* model (dashed line). Right: the specific angular momentum for the high-redshift galaxies in our MUSE and KMOS sample. We split the high-redshift sample into those galaxies with the best sampled dynamics/rotation curves (which we denote $q = 1$) and those with less well constrained rotation curves ($q = 2$). In the lower-right corner, we show the typical error bar, estimated using a combination of errors on the stellar mass, and uncertainties in the inclination and circular velocity measurement. We also include on the plot the unresolved galaxies from our sample using the limits on their sizes and velocity dispersions (the latter to provide an estimate of the upper limit on v_c). The median specific angular momentum (and bootstrap error) in bins of $\log_{10}(M_\star) = 0.3$ dex is also shown. The grey-scale shows the predicted distribution at $z \sim 1$ from the EAGLE simulation and we plot the median specific angular momentum in bins of stellar mass as well as the EAGLE $z = 0$ model from the left-hand panel. Although there is considerable scatter in the high-redshift galaxy sample, at $z \sim 1$, there are very few high-stellar-mass galaxies with specific angular momentum as large as comparably massive local spirals, suggesting that most of the accretion of high angular momentum material must occur below $z \sim 1$.

removes the implicit scaling between J and mass). The specific angular momentum is given by

$$j_\star = \frac{J}{M_\star} = \frac{\int_r (\boldsymbol{r} \times \bar{\boldsymbol{v}}) \rho_\star \, \mathrm{d}^3\boldsymbol{r}}{\int_r \rho_\star \, \mathrm{d}^3\boldsymbol{r}}, \quad (1)$$

where r and $\bar{v}(r)$ are the position and mean-velocity vectors (with respect to the centre of mass of the galaxy) and $\rho(r)$ is the three-dimensional density of the stars and gas.

To enable us to compare our results directly with similar measurements at $z \sim 0$, we take the same approximate estimator for specific angular momentum as used in Romanowsky & Fall (2012) [although see Burkert et al. (2016) for a more detailed treatment of angular momentum at high redshift]. In the local samples of Romanowsky & Fall (2012, see also Obreschkow et al. 2015), the scaling between specific angular momentum, rotational velocity and disc size for various morphological types is given by

$$j_n = k_n \, C_i \, v_s R_{1/2}, \quad (2)$$

where v_s is the rotation velocity at 2× the half-light radii ($R_{1/2}$) (which corresponds to $\simeq 3\, R_d$ for an exponential disc), $C_i = \sin^{-1}\theta_{im}$ is the deprojection correction factor (see Romanowsky & Fall 2012) and k_n depends on the Sérsic index (n) of the galaxy that can be approximated as

$$k_n = 1.15 + 0.029\, n + 0.062\, n^2. \quad (3)$$

For the galaxies with *HST* images, we run GALFIT to estimate the Sérsic index for the longest wavelength image available and derive a median Sérsic index of $n = 0.8 \pm 0.2$, with 90 per cent of the sample having $n < 2.5$, and therefore we adopt $j_\star = j_{n=1}$, which is applicable for exponential discs. Adopting a Sérsic index of $n = 2$ would result in a ∼20 per cent difference in $j_\star$. To infer the circular velocity, we measure the velocity from the rotation curve at 3 R_d (Romanowsky & Fall 2012). We report all of our measurements in Table A1.

In Fig. 8, we plot the specific angular momentum versus stellar mass for the high-redshift galaxies in our sample and compare to observations of spiral galaxies at $z = 0$ (Romanowsky & Fall 2012; Obreschkow & Glazebrook 2014). We split the high-redshift sample into those galaxies with the best sampled dynamics/rotation curves ($q = 1$) and those with less well constrained dynamics ($q = 2$). To ensure that we are not biased towards large/resolved galaxies in the high-redshift sample, we also include the unresolved galaxies, but approximate their maximum specific angular momentum by $j_\star = 1.3\, r_{1/2}\, \sigma$ (where σ is the velocity dispersion measured from the

collapsed, one-dimensional spectrum and is assumed to provide an upper limit on the circular velocity). The pre-factor of 1.3 is derived assuming a Sérsic index of $n = 1$–2 (Romanowsky & Fall 2012). We note that three of our survey fields (PKS1614−9323, Q2059−360 and Q0956+122) do not have extensive multi-wavelength imaging required to derive stellar masses and so do not include these galaxies on the plot.

3.8 EAGLE galaxy formation model

Before discussing the results from Fig. 8, we first need to test whether there may be any observational selection biases that may affect our conclusions. To achieve this, and aid the interpretation of our results, we exploit the hydrodynamic EAGLE simulation. We briefly discuss this simulation here, but refer the reader to Schaye et al. (2015, and references therein) for details. The Evolution and Assembly of GaLaxies and their Environments (EAGLE) simulations follow the evolution of dark matter, gas, stars and black holes in cosmological (10^6 Mpc^3) volumes (Crain et al. 2015; Schaye et al. 2015). The EAGLE reference model is particularly useful as it provides a reasonable match to the present-day galaxy stellar mass function, the amplitude of the galaxy–central black hole mass relation, and matches the $z \sim 0$ galaxy sizes and the colour–magnitude relations. With a reasonable match to the properties of the $z \sim 0$ galaxy population, EAGLE provides a useful tool for searching, and understanding, any observational biases in our sample and also for interpreting our results.

Lagos et al. (2017) show that the redshift evolution of the specific angular momentum of galaxies in the EAGLE simulation depends sensitively on mass and star formation rate cuts applied. For example, in the model, massive galaxies that are classified as 'passive' around $z \sim 0.8$ (those well below the 'main sequence') show little/no evolution in specific angular momentum from $z \sim 0.8$ to $z = 0$, whilst 'active' star-forming galaxies (i.e. on or above the 'main sequence') can increase their specific angular momentum[1] as rapidly as $j_\star/M_\star^{2/3} \propto (1+z)^{3/2}$. In principle, these predictions can be tested by observations.

From the EAGLE model, the most direct method for calculating angular momentum of galaxies is to sum the angular momentum of each star particle that is associated with a galaxy ($J_\mathrm{p} = \sum_i m_i\, \boldsymbol{r}_i \times \boldsymbol{v}_i$). However, this does not necessarily provide a direct comparison with the observation data, where the angular momentum is derived from the rotation curve and measured galaxy sizes. To ensure that a fair comparison between the observations and model can be made, we first calibrate the particle data in the EAGLE galaxies with their rotation curves. Schaller et al. (2015) extract rotation curves for EAGLE galaxies and show that over the radial range where the galaxies are well resolved, their rotation curves are in good agreement with those expected for observed galaxies of similar mass and bulge-to-disc ratio. We therefore select a subset of 5000 galaxies at $z \sim 0$ from the EAGLE simulation that have stellar masses between $M_\star = 10^8$ and $10^{11.5}$ M$_\odot$ and star formation rates of SFR = 0.1–50 M$_\odot$ yr^{-1} (i.e. reasonably well matched to the mass and star formation rate range of our observational sample) and derive their rotation curves. In this calculation, we adopt the minimum of their gravitational potential as the galaxy centre. We measure their stellar half-mass radii ($r_{1/2,\star}$), and the circular velocity from the rotation curve at 3 R_d and then compute the angular momentum from the rotation curve ($J_\mathrm{RC} = M_\star\, r_{1/2,\star}\, V(3\, R_\mathrm{d})$), and compare this to the angular momentum derived from the particle data (J_P). The angular momentum of the EAGLE galaxies[2] measured from the particular data (J_P) broadly agrees with that estimated from the rotation curves (J_RC), although fitting the data over the full range of J, we measure a sub-linear relation of $\log_{10}(J_\mathrm{RC}) = (0.87 \pm 0.10) \log_{10}(J_\mathrm{P}) + 1.75 \pm 0.20$. Although only a small effect, this sub-linear offset occurs due to two factors. First, the sizes of the low-mass galaxies become comparable to the ∼1 kpc gravitational softening length of the simulation; and secondly, at lower stellar masses, the random motions of the stars have a larger contribution to the total dynamical support. Nevertheless, in all of the remaining sections (and to be consistent with the observational data), we first calculate the 'particle' angular momentum of EAGLE galaxies and then convert these to the 'rotation curve' angular momentum.

To test how well the EAGLE model reproduces the observed mass–specific angular momentum sequence at $z = 0$, in Fig. 8 we plot the specific angular momentum ($j_\star = J/M_\star$) of ∼50 late- type galaxies from the observational study of Romanowsky & Fall (2012) and also include the observations of 16 nearby spirals from The H I Nearby Galaxy Survey (Walter et al. 2008) as discussed in Obreschkow & Glazebrook (2014). As discussed in Section 1, these local discs follow a correlation of $j_\star \propto M_\star^{2/3}$ with a scatter of $\sigma_{\log j} \sim 0.2$ dex. We overlay the specific angular momentum of galaxies at $z = 0$ from the EAGLE simulation, colour-coded by their rest-frame $(g-r)$ colour (Trayford et al. 2015). This highlights that the EAGLE model provides a reasonable match to the $z = 0$ scaling in $j_\star \propto M_\star^{2/3}$ in both normalization and scatter. Furthermore, the colour-coding highlights that, at fixed stellar mass, the blue star-forming galaxies (late types) have higher angular momentum compared to those with redder (early type) colours. A similar conclusion was reported by Zavala et al. (2016) who separated galaxies in EAGLE into early versus late types using their stellar orbits, identifying the same scaling between specific angular momentum and stellar mass for the late types. Lagos et al. (2017) also extend the analysis to investigate other morphological proxies such as spin, gas fraction, $(u-r)$ colour, concentration and stellar age and in all cases, the results indicate that galaxies that have low specific angular momentum (at fixed stellar mass) are gas-poor, red galaxies with higher stellar concentration and older mass-weighted ages.

In Fig. 8, we also show the predicted scaling between stellar mass and specific angular momentum from EAGLE at $z = 1$ after applying our mass and star formation rate limits to the galaxies in the model. This shows that EAGLE predicts the same scaling between specific angular momentum and stellar mass at $z = 0$ and 1 with $j_\star \propto M_\star^{2/3}$, with a change in normalization such that galaxies at $z \sim 1$ (at fixed stellar mass) have systematically lower specific angular momentum by ∼0.2 dex than those at $z \sim 0$. We will return to this comparison in Section 4.

Before discussing the high-redshift data, we note that one of the goals of the EAGLE simulation is to test sub-grid recipes for star formation and feedback. The sub-grid recipes in the EAGLE 'reference model' are calibrated to match the stellar mass function at $z = 0$, but this model is not unique. For example, in the reference model, the energy from star formation is coupled to the interstellar medium

[1] We note that in the angular momentum comparisons below, quantitatively similar results have been obtained from the Illustris simulation (Genel et al. 2015).

[2] We note that Lagos et al. (2017) show that in EAGLE the value of $J_\star$ and the scaling between $J_\star$ and stellar mass are insensitive to whether an aperture of 5 r_{50} or r_total is used.

(ISM) according to the local gas density and metallicity. This density dependence has the effect that outflows are able to preferentially expel material from centres of galaxies, where the gas has low angular momentum. However, as discussed by Crain et al. (2015), in other EAGLE models that also match the $z = 0$ stellar mass function, the energetics of the outflows are coupled to the ISM in different ways, with implications for the angular momentum. For example, in the *FBconst* model, the energy from star formation is distributed evenly into the surrounding ISM, irrespective of local density and metallicity. Since this model also matches the $z = 0$ stellar mass function, it is instructive to compare the angular momentum of the galaxies in this model to that in the reference model. In Fig. 8, we also overlay the $z = 0$ relation between the specific angular momentum ($j_\star$) and stellar mass ($M_\star$) in the EAGLE *FBconst* model. For stellar masses $M_\star \gtrsim 10^{10}$ M$_\odot$, the specific angular momenta of galaxies are a factor of ∼2 lower than those in the reference model. Since there is no dependence on outflow energetics with local density, this is a consequence of removing less low angular momentum material from the discs, which produces galaxies with specific angular momentum two times smaller than those in the reference model (Crain et al. 2015; Furlong et al. 2015). This highlights how observational constraints on the galaxy angular momentum can play a role in testing the sub-grid recipes used in numerical simulations.

3.9 Disc stability

In Section 4, we will investigate how the specific angular momentum is related to the galaxy morphologies. The 'disc stability' is intimately related to the galaxy morphologies, and so it is instructive to provide a crude (galaxy-integrated) measurement to aid the interpretation of these results. To define the disc stability, we use the Toomre parameter (Toomre 1964). In rotating disc of gas and stars, perturbations smaller than critical wavelength (λ_{max}) are stabilized against gravity by velocity dispersion whilst those larger than λ_{min} are stabilized by centrifugal force. The Toomre parameter is defined by $Q = \lambda_{min}/\lambda_{max}$, but can also be expressed as $Q = \sigma\kappa/(\pi G \Sigma_{gas})$, where σ is the radial velocity dispersion, Σ is the gas surface density and κ is the epicyclic frequency. If $Q < 1$, instabilities can develop on scales larger than the Jeans length and smaller than the maximal stability scale set by differential rotation. If $Q > 1$, then the differential rotation is sufficiently large to prevent large-scale collapse and no instabilities can develop.

To estimate the Toomre Q of each galaxy in our sample, we first estimate the gas surface density from the reddening-corrected star formation surface density (adopting the total star formation rate within 2 $r_{1/2}$ from Section 3.1) and use the Kennicutt–Schmidt relation (Kennicutt 1998) to infer Σ_{gas}. To estimate the epicyclic frequency of the disc (κ), we adopt the (inclination-corrected) rotational velocity at 3 R_d. We also calculate the (beam-smearing-corrected) velocity dispersion to measure σ. For the galaxies in our sample that are classified as rotationally supported, we derive a median Toomre Q of $Q = 0.80 \pm 0.10$ (with a full range of $Q = 0.08$–5.6). On average, these galaxies therefore have discs that are consistent with being marginally stable. This is not a surprising result for a high-redshift [O II] (i.e. star formation)-selected sample. For example, Hopkins (2012) shows that due to feedback from stellar winds, star-forming galaxies should be driven to the marginally stable threshold, in particular at high redshift where the galaxies have high gas fractions. In Fig. 9, we show the distribution of Toomre Q, split by V/σ. Although there are degeneracies between Q and V/σ, all of the sub-samples ($V/\sigma > 1$, 2 and 5) span the full range in Q, and the median Toomre Q increases with V/σ with $Q = 0.80 \pm 0.10$, 0.90 ± 0.08 and 1.30 ± 0.16 for $V/\sigma > 1$, 2 and 5, respectively. We will return to a discussion of this when comparing to the broad-band morphologies in Section 4.

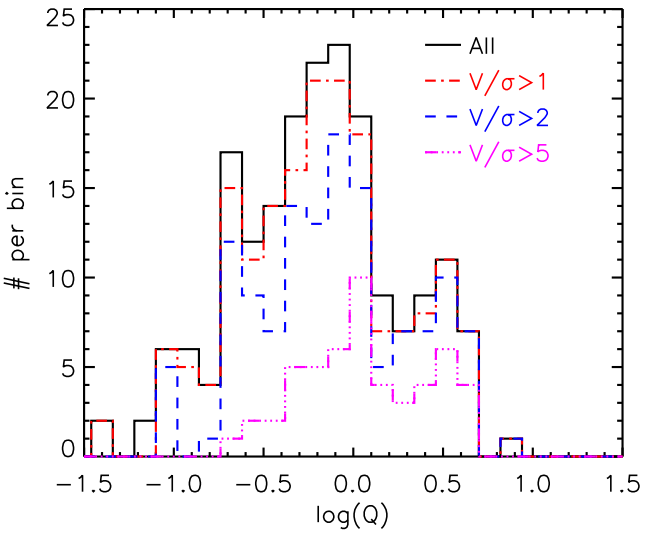

Figure 9. The distribution of Toomre Q for all galaxies in our sample that are classed as rotationally supported. We also sub-divide the sample by the ratio of rotational velocity to velocity dispersion (V/σ), with $V/\sigma > 1$, 2 and 5. The full range of Q for the whole sample is $Q = 0.08$–5.6, but with increasing V/σ, the median Toomre Q also increases to $Q = 0.80 \pm 0.10$, 0.80 ± 0.10, 0.90 ± 0.08 and 1.30 ± 0.16 for the full sample to $V/\sigma > 1$, 2 and 5, respectively.

Nevertheless, this observable provides a crude, but common way to classify the stability of the gas in a disc, and this will be important in comparison with the angular momentum. For example, in local galaxies, Cortese et al. (2016, using SAMI) and Lagos et al. (2017, using the EAGLE galaxy formation model) show that the disc stability and galaxy spin, λ_R (as defined in Emsellem et al. 2007), are strongly correlated with V/σ and define a continuous sequence in the specific angular momentum–stellar mass plane, where galaxies with high specific angular momentum are the most stable with high V/σ and λ_R. Moreover, Stevens, Croton & Mutch (2016, see also Obreschkow et al. 2015) suggest that specific angular momentum plays a major role in defining the disc stability. We will return to this in Section 4.

4 DISCUSSION

Observations of the sizes and rotational velocities of local spiral galaxies have suggested that ∼50 per cent of the initial specific angular momentum of the baryons within dark matter haloes must be lost due to viscous angular momentum redistribution and selective gas losses that occur as the galaxy forms and evolves.

In Fig. 8, we plot the specific angular momentum versus stellar mass for the high-redshift galaxies in our MUSE and KMOS sample. In this figure, we split the sample by their dynamics according to their ratio of V/σ (although we also highlight the galaxies whose dynamics most obviously display rotational support). We include the unresolved galaxies from our sample using the limits on their sizes and velocity dispersions (the latter to provide an estimate of the upper limit on V_c). In this figure, we also include the distribution (and median+scatter) at $z = 0$ and $z \sim 1$ from the EAGLE simulation.

Since there is considerable scatter in the data, we bin the specific angular momentum in stellar mass bins (using bins with

d $\log_{10}(M_\star) = 0.3$ dex) and overlay the median (and scatter in the distribution) in Fig. 8. Up to a stellar mass of $\sim 10^{10.5}$ $M_\odot$, the high-redshift galaxies follow a similar scaling between stellar mass and specific angular momentum as seen in local galaxies (see also Contini et al. 2016). Fitting the data over the stellar mass range $M_\star = 10^{8.5}$–$10^{11.5}$ $M_\odot$, we derive a scaling of $j_\star \propto M_\star^q$, with $q = 0.6 \pm 0.1$. Although the scaling $j_\star \propto M_\star^{2/3}$ is generally seen in local galaxies, when galaxies are split by morphological type, the power-law index varies between $q = 0.7$ and 1 (e.g. Cortese et al. 2016). However, the biggest difference between $z = 0$ and 1 is above a stellar mass of $M_\star \sim 10^{10.5}$ $M_\odot$, where the specific angular momentum of galaxies at $z \sim 1$ is $2.5 \pm 0.5\times$ lower than for comparably massive spiral galaxies at $z \sim 0$, and there are no galaxies in our observation sample with specific angular momentum as high as those of local spirals.

First, we note that this offset (and lack of galaxies with high specific angular momentum) does not appear to be driven by volume or selection effects that result in our observations missing high-stellar-mass, high-$j_\star$ galaxies. For example, although the local galaxy sample from Romanowsky & Fall (2012) is dominated by local ($D < 180$ Mpc) high-mass, edge-on spiral discs, the space density of star-forming galaxies with stellar mass $>10^{11}$ $M_\odot$ at $z \sim 1$ is $\sim 1.6 \times 10^{-3}$ Mpc^{-3} (Bundy, Ellis & Conselice 2005). The volume probed by the MUSE and KMOS observations is $\sim 1.5 \times 10^4$ Mpc^3 (comoving) between $z = 0.4$ and 1.2, and we expect $\sim 23 \pm 4$ such galaxies in our sample above this mass (and we detect 20). Thus, we do not appear to be missing a significant population of massive galaxies from our sample. At $z \sim 1$, we are also sensitive to star formation rates as low as ~ 4 $M_\odot$ yr^{-1} (given our typical surface brightness limits and adopting a median reddening of $A_V = 0.5$). This is below the so-called main sequence at this redshift since the star formation rate for a 'main-sequence' galaxy with $M_\star = 10^{11}$ $M_\odot$ at $z = 1$ is 100 $M_\odot$ yr^{-1} (Wuyts et al. 2013).

What physical processes are likely to affect the specific angular momentum of baryonic discs at high redshift (particularly those in galaxies with high stellar masses)? Due to cosmic expansion, a generic prediction of ΛCDM is that the relation between the mass and angular momentum of dark matter haloes changes with time. In a simple, spherically symmetric halo, the specific angular momentum, $j_h = J_h/M_h$, should scale as $j_h = M_h^{2/3}(1+z)^{-1/2}$ (e.g. Obreschkow et al. 2015), and if the ratio of the stellar to halo mass is independent of redshift, then the specific angular momentum of the baryons should scale as $j_\star \propto M_\star^{2/3}(1+z)^{-1/2}$. At $z \sim 1$, this simple model predicts that the specific angular momentum of discs should be $\sqrt{2}$ lower than at $z = 0$.

However, this 'closed-box' model does not account for gas inflows or outflows, and cosmologically based models have suggested that redshift evolution in $j_\star/M^{2/3}$ can evolve as rapidly as $(1+z)^{-3/2}$ from $z \sim 1$ to $z = 0$ (although this redshift evolution is sensitive to the mass and star formation rate limits applied to the selection of the galaxies; e.g. Lagos et al. 2017). For example, applying our mass and star formation rate limits to galaxies in the EAGLE model, galaxies at $z \sim 1$ are predicted to have specific angular momentum that is 0.2 dex (or a factor of ~ 1.6) lower than comparably massive galaxies at $z = 0$, although the most massive spirals at $z = 0$ have specific angular momentum that is ~ 3 times larger than any galaxies in our high-redshift sample.

The specific angular momentum of a galaxy can be increased or decreased depending on the evolution of the dark halo, the angular momentum and impact parameter of accreting material from the intergalactic medium, and how the star-forming regions evolve within the ISM. For example, if the impact parameter of accreting material is comparable to the disc radius (as suggested in some models; e.g. Dekel et al. 2009), then the streams gradually increase the specific angular momentum of the disc with decreasing redshift as the gas accretes on to the outer disc. The specific angular momentum can be further increased if the massive, star-forming regions (clumps) that form within the ISM torque and migrate inwards (since angular momentum is transferred outwards). However, galaxy average specific angular momentum can also be decreased if outflows (associated with individual clumps) drive gas out of the disc, and outflows with mass loading factors $\gg 1$ associated with individual star-forming regions (clumps) have been observed in a number of high-redshift galaxies (e.g. Genzel et al. 2011; Newman et al. 2012).

Since the galaxies in our sample span a range of redshifts, from $z \sim 0.3$–1.7, to test how the specific angular momentum evolves with time, we split our sample into four redshift bins. Whilst it has been instructive to normalize angular momentum by stellar mass ($j_\star = J/M_\star$), the stellar mass is an evolving quantity, and so we adopt the quantity $j_\star/M_\star^{2/3}$ (or equivalently, $J/M_\star^{5/3}$), and in Fig. 10 we compare the evolution of $j_\star/M_\star^{2/3}$ for our sample with late and early types at $z = 0$. This figure shows that there appears to be a trend of increasing specific angular momentum with decreasing redshift.

Before interpreting this plot in detail, first we note that Lagos et al. (2017) use EAGLE to show that the redshift evolution of $j_\star/M_\star^{2/3}$ is sensitive to the mass and star formation rate limits (see the 'Active' versus 'Passive' population in fig. 12 of Lagos et al. 2017). To test whether our results are sensitive to selection effects (in particular, the evolving mass limits may result in our observation missing low-stellar-mass galaxies at $z \sim 1$ that are detectable at $z \sim 0.3$), we select all of the galaxies from EAGLE between $z = 0.3$ and 1.5 whose star formation rates suggest that [O II] (or Hα) emission line fluxes (calculated using their star formation rate, redshift and adopting a typical reddening of $A_V = 0.5$) are above $f_{lim} = 1 \times 10^{-17}$ erg s^{-1} cm^{-2}. This flux limit corresponds approximately to the flux limit of our survey. We then apply mass cuts of $M_\star = 0.5$, 5 and 20×10^9 $M_\odot$ (which span the lower, median and upper quartiles of the stellar mass range in the observations). The stellar mass limits we applied to the EAGLE galaxies (which vary by a factor of 40 from 0.5 to 20×10^9 $M_\odot$) result in a change in the ratio of $j/M_\star^{2/3}$ of (a maximum of) 0.05 dex. Thus, the trend we see in $j/M^{2/3}$ with redshift does not appear to be driven by selection biases.

Thus, assuming that the majority of the rotationally supported high-redshift galaxies in our sample continue to evolve towards the spirals at $z \sim 0$, Fig. 10 suggests a change of $\Delta(j/M^{2/3}) \sim 0.4$ dex from $z \sim 1$ to $z \sim 0$. Equivalently, the evolution in $j_\star/M_\star^{2/3}$ is consistent with $j_\star/M_\star^{2/3} \propto (1+z)^{-n}$, with $n \sim -1$. In the right-hand panel of Fig. 10, we plot the data in linear time and overlay this redshift evolution. The evolution of $j_\star/M_\star^{2/3} \propto (1+z)^{-1}$ is consistent with that predicted for massive galaxies in EAGLE (galaxies in haloes with masses $M_{halo} = 10^{11.8\text{–}12.3}$ $M_\odot$; Lagos et al. 2017). In the figure, we also overlay tracks with $j_\star/M_\star^{2/3} \propto (1+z)^{-3/2}$ and $j_\star/M_\star^{2/3} \propto (1+z)^{-1/2}$ to show how the various predictions compare to the data.

Of course, the assumption that the rotationally supported 'discs' at $z \sim 1$ evolve into the rotationally supported spirals at $z \sim 0$ is difficult to test observationally. However, the model does allow us to measure how the angular momentum of individual galaxies evolves with time. To test how the angular momentum of today's spirals has evolved with time, and in particular what these evolved from $z \sim 1$, we identify all of the galaxies in EAGLE whose (final) $j_\star/M_\star^{2/3}$ is consistent with today's early and late types ($j_\star/M_\star^{2/3} = -3.82 \pm 0.05$

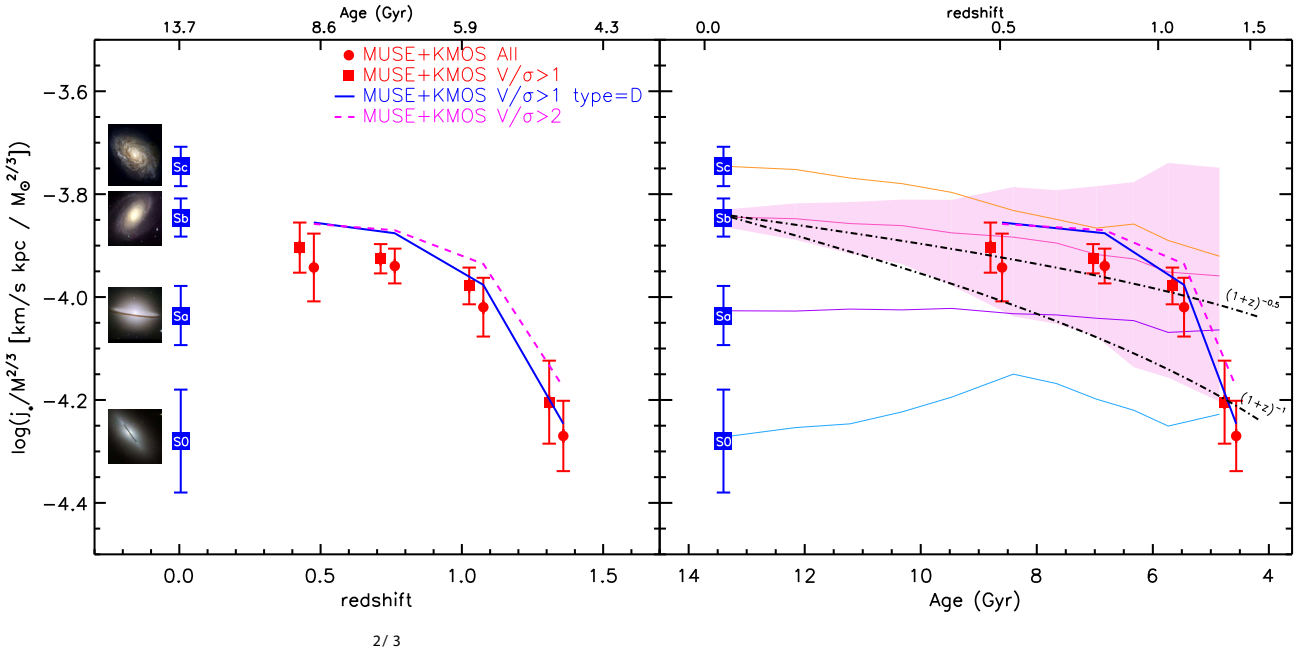

Figure 10. Left: redshift evolution of the $j_\star/M_\star^{2/3}$ from $z = 0$ to $z \sim 1.5$. We split the $z = 0$ galaxies from Romanowsky & Fall (2012) into their types (from S0 to Sd). Data points and their error bars in all of the observational points denote the bootstrap median and scatter in the distribution. Right: the average evolution of individual galaxies in the EAGLE simulation (observational data is the same as in the left-hand panel). We identify all galaxies in EAGLE that have angular momentum consistent with late- and early-type galaxies at $z = 0$ and use the merger trees to measure the ratio of $j_\star/M_\star^{2/3}$ of the main progenitor galaxy with redshift. We show the typical evolution and the scatter (68 per cent) by the shaded region. In EAGLE, above $z \sim 1.5$, the angular momentum of the model early and late types is similar, but below $z \sim 1.5$, the ratio of $j_\star/M_\star^{2/3}$ grows by ∼60 per cent due to a combination of gas accretion and outflows (which preferentially expel low angular momentum material). In comparison, the angular momentum of the galaxies that end up as early types at $z = 0$ remains approximately constant over the same period. We also overlay a track of $j_\star/M_\star^{2/3} \propto (1 + z)^{-n}$, with $n = 0.5$ and 1.5. The former represents the evolution if the angular momentum grows linearly with time.

and -4.02 ± 0.05, respectively) and trace the evolution of their angular momentum with redshift (using the main sub-halo progenitor in each case to trace their dynamics). We show these evolutionary tracks in Fig. 10. In the EAGLE simulation, early-type galaxies at $z = 0$ have an approximately constant $j_\star/M_\star^{2/3}$ from $z \sim 1$. This is similar to the findings of Lagos et al. (2017) who show that galaxies with mass-weighted ages $\gtrsim$9 Gyr have constant $j_\star/M^{2/3}$ with redshift below $z \sim 2$. In contrast, the model predicts that spiral galaxies at $z \sim 0$ have gradually increased their specific angular momentum from high redshift, and indeed, for our observed sample, that the angular momentum of galaxies follows $j_\star/M_\star^{2/3} \propto (1 + z)^{-1}$ (see also Fig. 8). Thus, in the models, the specific angular momentum of today's spirals was $\sim 2.5\times$ lower than that at $z = 0$. The increase in $j_\star/M_\star^{2/3}$ has been attributed to the age at which dark matter haloes cease their expansion (their so-called turnaround epoch) and the fact that star-forming gas at late times has high specific angular momentum that impacts the disc at large radii (e.g. see fig. 13 of Lagos et al. 2017).

It is useful to investigate the relation between the angular momentum, stability of the discs and the star formation rate (or star formation surface density). As we discussed in Section 3.9, the stability of a gas disc against clump formation is quantified by the Toomre parameter, Q. Recently, Obreschkow et al. (2015) suggested that the low angular momentum of high-redshift galaxies is the dominant driver of the formation of 'clumps', which hence leads to clumpy/disturbed morphologies and intense star formation. As the specific angular momentum increases with decreasing redshift, the disc-average Toomre Q becomes greater than unity and the disc becomes globally stable.

To test whether this is consistent with the galaxies in our sample, we select all the rotationally supported galaxies from our MUSE and KMOS survey that have stellar masses greater than $M_\star = 10^{10}$ M$_\odot$, and split the sample into galaxies above and below $j_\star/M_\star^{2/3} = 10^{2.5}$ km s^{-1} kpc M$_\odot^{-2/3}$ (we only consider galaxies above $M_\star = 10^{10}$ M$_\odot$ since these are well resolved in our data). For these two sub-samples, we derive $Q = 1.10 \pm 0.18$ for the galaxies with the highest $j_\star/M_\star^{2/3}$ and $Q = 0.53 \pm 0.22$ for those galaxies with the lowest $j_\star/M_\star^{2/3}$. This is not a particularly surprising result since the angular momentum and Toomre Q are both a strong function of rotational velocity and radius. However, it is interesting to note that the average star formation rate and star formation surface densities of these two subsets of high and low $j_\star/M^{2/3}$ are also markedly different. For the galaxies above the $j_\star/M^{2/3}$ sequence at this mass, the star formation rates and star formation surface densities are SFR $= 8 \pm 4$ M$_\odot$ yr^{-1} and $\Sigma_{\rm SFR} = 123 \pm 23$ M$_\odot$ yr^{-1} kpc^2, respectively. In comparison, the galaxies below the sequence have higher rates, with SFR $= 21 \pm 4$ M$_\odot$ yr^{-1} and $\Sigma_{\rm SFR} = 206 \pm 45$ M$_\odot$ yr^{-1} kpc^2, respectively. In this comparison, the star formation rates are the most illustrative indication of the difference in sub-sample properties since they are independent of $j_\star$, stellar mass and size.

Since a large fraction of our sample have been observed using *HST*, we can also investigate the morphologies of those galaxies above and below the specific angular momentum–stellar mass sequence. In Fig. 11, we show *HST* colour images of 14 galaxies, 7 each with specific angular momentum ($j_\star$) that are above or below the $j_\star$–$M_\star$ sequence. We select galaxies for this plot that are matched in redshift and stellar mass [all have stellar masses $>2 \times 10^9$ M$_\odot$,

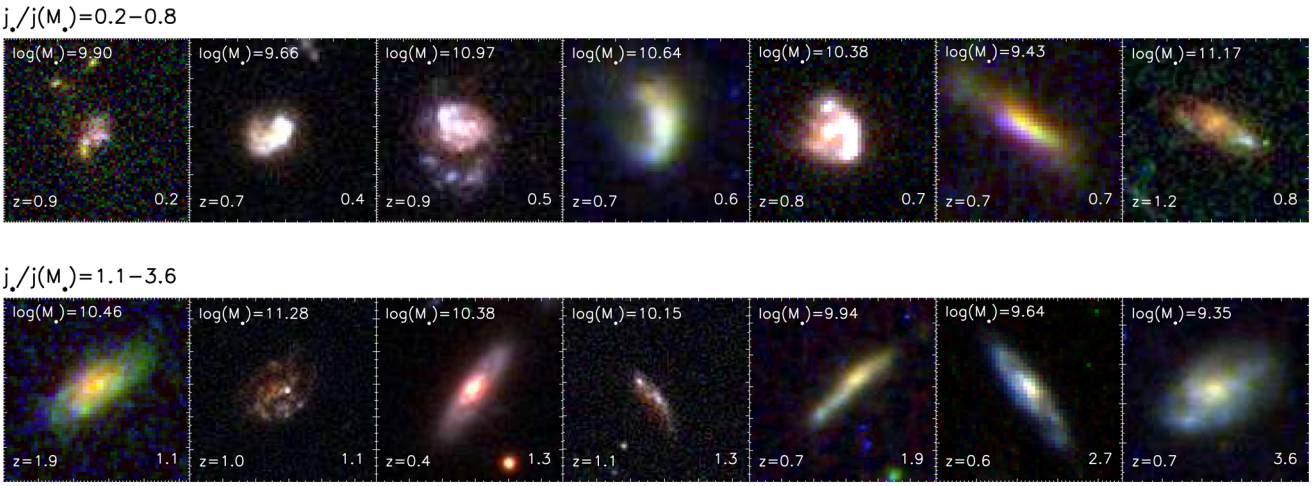

Figure 11. *HST* colour images of 14 galaxies from Fig. 8 whose specific angular momenta ($j_\star$) are above the $j_\star$–$M_\star$ sequence (upper row) and below the $j_\star$–$M_\star$ sequence (lower row). The galaxies shown in this figure all have stellar masses $>2 \times 10^9$ $M_\odot$, with similar stellar masses and redshift distributions ($\log_{10}(M_\star/M_\odot) = 10.3 \pm 0.4$ and 10.2 ± 0.3 and $z = 0.78 \pm 0.10$ and 0.74 ± 0.11, respectively, for the upper and lower rows). The stellar masses and redshifts are given in the upper-left and lower-left corners, respectively. The value in the lower-right corner of each image is the fractional offset from the $j_\star$–$M_\star$ sequence in Fig. 8 (i.e. a value of 0.2 means that galaxy has a specific angular momentum that is five times lower than the $j_\star$–$M_\star$ sequence given its stellar mass). These images demonstrate that galaxies with lower specific angular momentum (at fixed mass) are those with more disturbed morphologies and larger and brighter clumps (upper row), whilst the galaxies with high angular momentum are those with morphologies that more closely resemble spiral galaxies (lower row). The galaxies with low specific angular momentum are also dynamically unstable, with Toomre $Q = 0.53 \pm 0.22$ compared to those with high specific angular momentum that have Toomre $Q = 1.10 \pm 0.18$. Together, this demonstrates that the disc stability and morphology of the galaxies are strongly correlated with the angular momentum of the gas disc.

with medians of $\log_{10}(M_\star/M_\odot) = 10.3 \pm 0.4$ and 10.2 ± 0.3 and $z = 0.78 \pm 0.10$ and 0.74 ± 0.11, respectively, for the upper and lower rows). Whilst a full morphological analysis is beyond the scope of this paper, it appears from this plot that the galaxies with higher specific angular momentum (at fixed mass) are those with more established (smoother) discs. In contrast, the galaxies with lower angular momentum are those with morphologies that are either more compact, more disturbed morphologies and/or larger and brighter clumps.

Taken together, these results suggest that at $z \sim 1$, galaxies follow a similar scaling between mass and specific angular momentum as those at $z \sim 0$. However, at high masses ($>M_\star$ at $z \sim 1$), star-forming galaxies have lower specific angular momentum (by a factor of ∼2.5) than a mass matched sample at $z \sim 0$, and we do not find any high-redshift galaxies with specific angular momentum as high as those in local spirals. From their Toomre stability and star formation surface densities, the most unstable discs have the lowest specific angular momentum, asymmetric morphologies and highest star formation rate surface densities (see also Obreschkow et al. 2015). Galaxies with higher specific angular momentum appear to be more stable, with smoother (disc-like) morphologies.

Finally, we calculate the distribution of baryonic spins for our sample. The spin typically refers to the fraction of centrifugal support for the halo. Both linear theory and *N*-body simulations have suggested that haloes have spins that follow approximately lognormal distributions with average value $\lambda_{DM} = 0.035$ (Bett et al. 2007, i.e. only ∼3.5 per cent of the dynamical support of a halo is centrifugal, the rest comes from dispersion). To estimate how the disc and halo angular momentum are related, we calculate the spin of the disc, λ, as $\lambda = \sqrt{2}/0.1\ R_d\ H(z)/V(3\ R_d)$, where $H(z) = H_0(\Omega_{\Lambda,0} + \Omega_{m,0}(1+z)^3)^{0.5}$. This is the simplest approach that assumes that the galaxy is embedded inside an isothermal spherical CDM haloes (e.g. White 1984; Mo et al. 1998) that are truncated at the virial radius (Peebles 1969, see Burkert et al. 2016 for a discussion for the results from adopting more complex halo profiles). In Fig. 12, we plot the distribution of $\lambda \times (j_d/j_{DM})$ for our sample. If the initial halo and baryonic angular momentum are similar, i.e. $j_{DM} \simeq j_d$, this quantity reflects the fraction of angular momentum lost during the formation of $z \sim 1$ star-forming galaxies. In this figure, we split the sample into four categories: all galaxies with disc-like dynamics with $V/\sigma > 1$, 2 and 5. We fit these distributions with a lognormal power-law distribution, deriving best-fitting parameters in $[\lambda', \sigma]$ of $[0.040 \pm 0.002, 0.45 \pm 0.05]$,

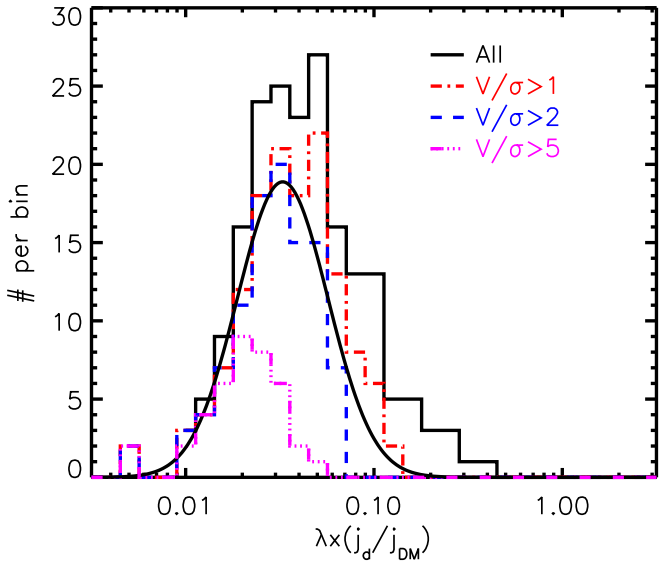

Figure 12. The distribution of spin ($\lambda \times (j_d/j_{DM})$) for the galaxies in our sample. We split the sample into four categories: all rotationally supported systems, and those with $V/\sigma > 1$, 2 and 5. We fit the distribution of galaxies with $V/\sigma > 2$ with a power-law relation to derive best-fitting parameters $\lambda' = 0.040 \pm 0.002$ and $\sigma = 0.045 \pm 0.005$.

[0.041 ± 0.002, 0.42 ± 0.05] and [0.068 ± 0.002, 0.50 ± 0.04], respectively.

An alternative approach (see also Harrison et al. 2017) is to assume the spin for the baryons of $\lambda' = 0.035$ and calculate the fraction of angular momentum that has been retained (assuming $j_{\rm DM} \simeq j_{\rm d}$ initially). For the galaxies that appear to be rotationally supported with ratios of $V/\sigma > 1$, 2 and 5, we derive median values of $j_{\rm d}/j_{\rm DM} \sim 1.18 \pm 0.10, 0.95 \pm 0.06$ and 0.70 ± 0.05 (bootstrap errors). Since these spins are similar to the halo ($\lambda = 0.035$), this suggests that the angular momentum of 'rotationally supported' galaxies at $z \sim 1$ broadly follows that expected from theoretical expectation from the halo, with most of the angular momentum retained during the (initial) collapse. Equivalently, for the galaxies with the highest ratio of V/σ (which are also those with the highest specific angular momentum and latest morphological types; see Fig. 11), the fraction of angular momentum retained must be $\gtrsim$70 per cent.

5 CONCLUSIONS

Exploiting MUSE and KMOS observations, we study the dynamics of 405 star-forming galaxies across the redshift range $z = 0.28$–1.65, with a median redshift of $z = 0.84$. From estimates of their stellar masses and star formation rates, our sample appear to be representative of the star-forming 'main sequence' from $z = 0.3$ to 1.7, with ranges of SFR $= 0.1$–$30\,{\rm M}_\odot\,{\rm yr}^{-1}$ and $M_\star = 10^8$–$10^{11}\,{\rm M}_\odot$.

Our main results are summarized as follows.

(i) From the dynamics and morphologies of the galaxies in the sample, 49 ± 4 per cent appear to be rotationally supported, 24 ± 3 per cent are unresolved and only ∼5 ± 2 per cent appear to be major mergers. The remainder appear to be irregular (or perhaps face-on) systems. Our estimate of the 'disc' fraction in this sample is consistent with other dynamical studies over a similar redshift range that have also found that rotationally supported systems make up ∼40–70 per cent of the star-forming population.

(ii) We measure half-light sizes of the galaxies in both the broad-band continuum images (using *HST* imaging in many cases) and in the nebular emission lines. The nebular emission line sizes are typically a factor of 1.18 ± 0.03 larger than the continuum sizes. This is consistent with recent results from the 3D *HST* survey that has also shown that the nebular emission from $\sim L^\star$ star-forming galaxies at $z \sim 1$ is systematically more extended than the stellar continuum.

(iii) For those galaxies whose dynamics resemble rotationally supported systems, we simultaneously fit the imaging and dynamics with a disc + halo model to derive the best-fitting structural parameters (such as disc inclination, position angle, [*x*/*y*] centre, disc mass, disc size, dark matter core radius and density). The dynamical and morphological major axes are typically misaligned by Δ PA $= 9\overset{\circ}{.}5 \pm 0\overset{\circ}{.}5$, which we attribute to the dynamical 'settling' of the gas and stars as the discs evolve.

(iv) We combine the inclination-corrected rotational velocities with the galaxy sizes and intrinsic velocity dispersions to investigate the global stability of the gas discs. For the galaxies that are classified as rotationally supported, we derive a median Toomre Q of $Q = 0.80 \pm 0.10$. This is consistent with numerical models that predict that in high-redshift, gas-rich galaxies the discs are maintained at the marginally stable threshold due to the feedback from stellar winds that arrest collapse (e.g. Hopkins 2012).

(v) We use the galaxy sizes, rotation speeds and stellar masses to investigate how the specific angular momentum of gas discs evolves with cosmic time. We show that the galaxies in our sample (which have a median redshift of $z = 0.84 \pm 0.03$) follow a similar scaling between stellar mass and specific angular momentum as local galaxies. Fitting the data over the stellar mass range $M_\star = 10^{8.5}$–$10^{11.5}\,{\rm M}_\odot$ suggests $j_\star \propto M_\star^q$, with $q = 0.6 \pm 0.1$. However, at $z = 1$, we do not find any galaxies with specific angular momentum as high as those of local spirals. Thus, the most massive star-forming discs at $z \sim 0$ must have increased their specific angular momentum (by a factor of ∼3) between $z \sim 1$ and $z \sim 0$.

(vi) To account for the evolving stellar masses of galaxies, we measure the ratio of $j_\star/M_\star^{2/3}$ and split our observed sample into four redshift bins between $z = 0.3$ and 1.5. For a star formation-selected (and mass-limited) sample, we show that the specific angular momentum evolves with redshift as $j_\star \propto M_\star^{2/3}(1+z)^{-1}$, which is similar to that predicted by the latest numerical models, which also suggest that spiral galaxies at $z \sim 0$ appear to have gradually increased their specific angular momentum from high redshift (in contrast to 'passive' galaxies at $z \sim 0$ that, on average, have near-constant specific angular momentum between $z \sim 0$ and $z \sim 1$).

(vii) Combining the measurements of the angular momentum, star formation surface density and disc stability, we show that galaxies with stellar masses greater than $M_\star = 10^{10}\,{\rm M}_\odot$ with the highest $j_\star/M_\star^{2/3}$ are the most stable, with discs with Toomre $Q = 1.20 \pm 0.20$, compared to $Q = 0.51 \pm 0.17$ for galaxies above and below $j_\star/M_\star^{2/3} = 10^{2.5}\,{\rm km\,s^{-1}\,kpc\,M_\odot^{-2/3}}$, respectively. Since $j_\star$ and Q are both functions of size and rotational velocity, we also measure the average star formation rate and star formation surface densities of these two subsets of high- and low-$j_\star/M^{2/3}$ galaxies. These sub-samples are markedly different, with a median $\Sigma_{\rm SFR} = 123 \pm 23$ and $206 \pm 45\,{\rm M}_\odot\,{\rm yr}^{-1}$ for those galaxies above and below the fiducial $j_\star/M_\star^{2/3}$ relation respectively. In terms of star formation rates alone, there is a similar difference, with SFR $= 8 \pm 4$ and $21 \pm 4\,{\rm M}_\odot\,{\rm yr}^{-1}$ above and below the sequence, respectively.

(viii) At a fixed mass, we show that galaxies with high specific angular momentum ($j_\star$; i.e. those above the $j_\star$–$M_\star$) relation are those with morphologies that more closely resemble spiral galaxies, with bigger bulges and smoother discs. In contrast, galaxies with lower specific angular momentum (at fixed mass) are those with more disturbed, asymmetric morphologies, larger and brighter clumps.

(ix) Finally, we show that the distribution of spins for the rotationally supported galaxies in our sample is similar to that expected for the haloes. For example, for galaxies that have disc like dynamics and $V/\sigma > 2$, we derive $\lambda' = 0.040 \pm 0.002$ and $\sigma = 0.45 \pm 0.05$. This suggests that the angular momentum of 'rotationally supported' galaxies at $z \sim 1$ broadly follows that expected from theoretical expectation from the halo, with most of the angular momentum retained during the (initial) collapse.

Overall, our results show that star-forming discs at $z \sim 1$ have lower specific angular momentum than a stellar mass matched sample at $z \sim 0$. At high redshift, the fraction of rotationally supported 'disc' galaxies is high, yet most of these galaxies appear irregular/clumpy. This appears to be due to the low angular momentum that results in globally unstable, turbulent systems. Indeed, specific angular momentum appears to play a major role in defining the disc stability, star formation surface densities and morphology. As the specific angular momentum of growing discs increases below $z \sim 1$, the galaxy discs must evolve from globally unstable clumpy, turbulent systems into stable, flat regular spirals.

ACKNOWLEDGEMENTS

We thank the anonymous referee for their constructive report that significantly improved the content and clarity of this work. AMS gratefully acknowledges an STFC Advanced Fellowship

through grant number ST/H005234/1, the Leverhulme foundation and STFC grant ST/L00075X/1. IRS acknowledges support from STFC (ST/L00075X/1), the ERC Advanced Investigator programme 321334-DUSTYGAL and a Royal Society/Wolfson Merit Award. JS and RB acknowledge ERC advanced grants 278594-GasAroundGalaxies and 339659-MUSICOS, respectively. DS acknowledges financial support from the Netherlands Organisation for Scientific Research (NWO) through a Vani fellowship and from an FCT investigator starting grant (IF/01154/2012/CP0189/CT0010). RAC acknowledges a Royal Society University Research Fellowship.

REFERENCES

Bacon R. et al., 2010, in Proc. SPIE, Vol. 7735, Ground-based and Airborne Instrumentation for Astronomy III. SPIE, Bellingham, p. 773508
Bacon R. et al., 2015, A&A, 575, A75
Barnes J., Efstathiou G., 1987, ApJ, 319, 575
Bell E. F. et al., 2004, ApJ, 600, L11
Bertin E., Arnouts S., 1996, A&AS, 117, 393
Bertola F., Capaccioli M., 1975, ApJ, 200, 439
Bett P., Eke V., Frenk C. S., Jenkins A., Helly J., Navarro J., 2007, MNRAS, 376, 215
Bolzonella M., Miralles J.-M., Pelló R., 2000, A&A, 363, 476
Brammer G. B., van Dokkum P. G., Coppi P., 2008, ApJ, 686, 1503
Bruce V. A. et al., 2014, MNRAS, 444, 1660
Buitrago F., Trujillo I., Conselice C. J., Häußler B., 2013, MNRAS, 428, 1460
Bundy K., Ellis R. S., Conselice C. J., 2005, ApJ, 625, 621
Burkert A., 1995, ApJ, 447, L25
Burkert A., 2009, in Jogee S., Marinova I., Hao L., Blanc G. A., eds, ASP Conf. Ser. Vol. 419, Galaxy Evolution: Emerging Insights and Future Challenges. Astron. Soc. Pac., San Francisco, p. 3
Burkert A. et al., 2016, ApJ, 826, 214
Calzetti D., Armus L., Bohlin R. C., Kinney A. L., Koornneef J., Storchi-Bergmann T., 2000, ApJ, 533, 682
Catelan P., Theuns T., 1996, MNRAS, 282, 436
Ceverino D., Dekel A., Bournaud F., 2010, MNRAS, 404, 2151
Ciardullo R. et al., 2013, ApJ, 769, 83
Cole S., Lacey C., 1996, MNRAS, 281, 716
Conselice C. J., Bluck A. F. L., Ravindranath S., Mortlock A., Koekemoer A. M., Buitrago F., Grützbauch R., Penny S. J., 2011, MNRAS, 417, 2770
Contini T. et al., 2016, A&A, 591, A49
Cortese L. et al., 2016, MNRAS, 463, 170
Courteau S., 1997, AJ, 114, 2402
Crain R. A. et al., 2015, MNRAS, 450, 1937
Danovich M., Dekel A., Hahn O., Ceverino D., Primack J., 2015, MNRAS, 449, 2087
Dekel A., Sari R., Ceverino D., 2009, ApJ, 703, 785
Emsellem E. et al., 2007, MNRAS, 379, 401
Epinat B. et al., 2012, A&A, 539, A92
Fall S. M., 1983, in Athanassoula E., ed., Proc. IAU Symp. 100, Internal Kinematics and Dynamics of Galaxies. Reidel, Dordrecht, p. 391
Fall S. M., Romanowsky A. J., 2013, ApJ, 769, L26
Ferguson H. C. et al., 2004, ApJ, 600, L107
Förster Schreiber N. M. et al., 2009, ApJ, 706, 1364
Franx M., Illingworth G., de Zeeuw T., 1991, ApJ, 383, 112
Freeman K. C., 1970, ApJ, 160, 811
Furlong M. et al., 2015, MNRAS, 450, 4486
Gallagher J. S., III, Hunter D. A., 1984, ARA&A, 22, 37
Geach J. E., Smail I., Best P. N., Kurk J., Casali M., Ivison R. J., Coppin K., 2008, MNRAS, 388, 1473
Genel S., Fall S. M., Hernquist L., Vogelsberger M., Snyder G. F., Rodriguez-Gomez V., Sijacki D., Springel V., 2015, ApJ, 804, L40
Genzel R. et al., 2011, ApJ, 733, 101
Giavalisco M., Steidel C. C., Macchetto F. D., 1996, ApJ, 470, 189
Gnerucci A. et al., 2011, A&A, 528, A88
Guo Y. et al., 2009, MNRAS, 398, 1129
Harrison C. M. et al., 2017, MNRAS, preprint (arXiv:1701.05561)
Hopkins P. F., 2012, MNRAS, 423, 2016
Husband K., Bremer M. N., Stanway E. R., Lehnert M. D., 2015, MNRAS, 452, 2388
Kennicutt R. C., Jr, 1998, ApJ, 498, 541
Khostovan A. A., Sobral D., Mobasher B., Best P. N., Smail I., Stott J. P., Hemmati S., Nayyeri H., 2015, MNRAS, 452, 3948
Kriek M., van Dokkum P. G., Labbé I., Franx M., Illingworth G. D., Marchesini D., Quadri R. F., 2009, ApJ, 700, 221
Lagos C. d. P., Theuns T., Stevens A. R. H., Cortese L., Padilla N. D., Davis T. A., Contreras S., Croton D., 2017, MNRAS, 464, 3850
Law D. R., Steidel C. C., Erb D. K., Larkin J. E., Pettini M., Shapley A. E., Wright S. A., 2009, ApJ, 697, 2057
Leitherer C. et al., 1999, ApJS, 123, 3
Ly C. et al., 2007, ApJ, 657, 738
Mo H. J., Mao S., White S. D. M., 1998, MNRAS, 295, 319
Morishita T., Ichikawa T., Kajisawa M., 2014, ApJ, 785, 18
Mortlock A. et al., 2013, MNRAS, 433, 1185
Muzzin A. et al., 2013, ApJS, 206, 8
Navarro J. F., Frenk C. S., White S. D. M., 1997, ApJ, 490, 493
Nelson E. J. et al., 2016, ApJ, 828, 27
Newman S. F. et al., 2012, ApJ, 761, 43
Obreschkow D., Glazebrook K., 2014, ApJ, 784, 26
Obreschkow D. et al., 2015, ApJ, 815, 97
Oesch P. A. et al., 2010, ApJ, 714, L47
Peebles P. J. E., 1969, ApJ, 155, 393
Peng C. Y., Ho L. C., Impey C. D., Rix H.-W., 2002, AJ, 124, 266
Persic M., Salucci P., 1988, MNRAS, 234, 131
Puech M. et al., 2008, A&A, 484, 173
Richard J. et al., 2015, MNRAS, 446, L16
Roberts M. S., 1963, ARA&A, 1, 149
Romanowsky A. J., Fall S. M., 2012, ApJS, 203, 17
Salucci P., Burkert A., 2000, ApJ, 537, L9
Sandage A., 1986, A&A, 161, 89
Sandage A., Freeman K. C., Stokes N. R., 1970, ApJ, 160, 831
Schaller M. et al., 2015, MNRAS, 452, 343
Schaye J. et al., 2015, MNRAS, 446, 521
Sharples R. M. et al., 2004, in Moorwood A. F. M., Iye M., eds, Proc. SPIE, Vol. 5492, Ground-based Instrumentation for Astronomy. SPIE, Bellingham, p. 1179
Sobral D. et al., 2009, MNRAS, 398, 75
Sobral D., Smail I., Best P. N., Geach J. E., Matsuda Y., Stott J. P., Cirasuolo M., Kurk J., 2013a, MNRAS, 428, 1128
Sobral D. et al., 2013b, ApJ, 779, 139
Sobral D. et al., 2015, MNRAS, 451, 2303
Steinmetz M., Bartelmann M., 1995, MNRAS, 272, 570
Stevens A. R. H., Croton D. J., Mutch S. J., 2016, MNRAS, 461, 859
Stott J. P. et al., 2014, MNRAS, 443, 2695
Stott J. P. et al., 2016, MNRAS, 457, 1888
Tadaki K. et al., 2017, ApJ, 834, 135
Toomre A., 1964, ApJ, 139, 1217
Trayford J. W. et al., 2015, MNRAS, 452, 2879
van der Wel A. et al., 2014, ApJ, 788, 28
Walter F., Brinks E., de Blok W. J. G., Bigiel F., Kennicutt R. C., Jr, Thornley M. D., Leroy A., 2008, AJ, 136, 2563
White S. D. M., 1984, ApJ, 286, 38
Wisnioski E. et al., 2015, ApJ, 799, 209
Wuyts S. et al., 2013, ApJ, 779, 135
Zavala J. et al., 2016, MNRAS, 460, 4466

SUPPORTING INFORMATION

Supplementary data are available at *MNRAS* online.

Supplementary_Table.tex
Supplementary_Table.asc
Supplementary_Figures.tar.gz

[1]*Institute for Computational Cosmology, Durham University, South Road, Durham DH1 3LE, UK*
[2]*Center for Extragalactic Astronomy, Durham University, South Road, Durham DH1 3LE, UK*
[3]*Leiden Observatory, Leiden University, PO Box 9513, NL-2300 RA Leiden, the Netherlands*
[4]*CRAL, Observatoire de Lyon, Universite Lyon 1, 9 Avenue Ch. Andre, F-69561 Saint Genis Laval Cedex, France*
[5]*IRAP, Institut de Recherche en Astrophysique et Planetologie, CNRS, 14, avenue Edouard Belin, F-31400 Toulouse, France*
[6]*Universite de Toulouse, UPS-OMP, 14, avenue Edouard Belin, F-31400 Toulouse, France*
[7]*Astrophysics Research Institute, Liverpool John Moores University, 146 Brownlow Hill, Liverpool L3 5RF, UK*
[8]*European Southern Observatory, Karl Schwarzschild Straße 2, D-85748 Garching, Germany*
[9]*Max-Planck-Institut für Astronomie, Königstuhl 17, D-69117 Heidelberg, Germany*
[10]*Aix Marseille Université, CNRS, LAM, Laboratoire d'Astrophysique de Marseille, UMR 7326, F-13388 Marseille, France*
[11]*INAF, Osservatorio di Roma, via Frascati 33, I-00040 Monteporzio, Italy*
[12]*International Centre for Radio Astronomy Research (ICRAR), M468, University of Western Australia, 35 Stirling Hwy, Crawley, WA 6009, Australia*
[13]*Australian Research Council Centre of Excellence for All-sky Astrophysics (CAASTRO), 44 Rosehill Street Redfern, NSW 2016, Australia*
[14]*Kavli Institute for Theoretical Physics, Kohn Hall, University of California, Santa Barbara, CA 93106, USA*
[15]*Department of Physics, Lancaster University, Lancaster LA1 4BY, UK*
[16]*Sub-department of Astrophysics, University of Oxford, Denys Wilkinson Building, Keble Road, Oxford OX1 3RH, UK*

This paper has been typeset from a TEX/LATEX file prepared by the author.